Lehigh University
Lehigh Preserve

Theses and Dissertations

2012

# Computational Fluid Dynamic Simulation for an Offshore Wind Turbine

Chenglong Wang
*Lehigh University*

Follow this and additional works at: http://preserve.lehigh.edu/etd

Recommended Citation
Wang, Chenglong, "Computational Fluid Dynamic Simulation for an Offshore Wind Turbine" (2012). *Theses and Dissertations.* Paper 1153.

This Thesis is brought to you for free and open access by Lehigh Preserve. It has been accepted for inclusion in Theses and Dissertations by an authorized administrator of Lehigh Preserve. For more information, please contact preserve@lehigh.edu.

# Computational Fluid Dynamic Simulation for an Offshore Wind Turbine

by

CHENGLONG WANG

A Thesis

Presented to the Graduate and Research Committee

of Lehigh University

in Candidacy for the Degree of

Master of Science

In

Mechanical Engineering and Mechanics

Lehigh University

September 2011

This thesis is accepted and approved in partial fulfillment of the requirements for the Master of Science.

_____

Date

_____

Thesis Advisor

_____

Chairperson of Department

# ACKNOWLEDGMENTS

Without the help from my advisor, Professor Alparslan Oztekin of Lehigh University, I would not be able to start my research on wind energy. His encouragement and guidance has inspired me with great interest on the simulation of wind turbine. From his strong background of computational fluid dynamics, I have a better understanding about the wake of single wind turbine.

Besides my advisor, I would like to appreciate the help from Ming-Chen Hsu, PhD of University of California, San Diego. Because of his generous instruction including the design of the rotor blade and the simulation on the whole fluid domain, I could go through all these materials to complete this thesis in this short time.

I also wish to thank Haolin Ma and W. Chris Schleicher at our offices in Packard Lab for their enthusiasm and helpful expertise in computational fluid dynamics. Thanks to their kindness and creative enlightenment, I could always concentrate on my research full of passion and intensity.

# Table of Contents

ACKNOWLEDGMENTS ..... III

Table of Contents ..... IV

List of Figures ..... VI

ABSTRACT ..... 1

1. Introduction ..... 2

2. Mathematical Model ..... 5

2.1 Large Eddy Simulation (LES) Model ..... 5

2.2 Subgrid-Scale Model ..... 6

3. Wind Turbine Rotor ..... 9

3.1 Rotor Blade ..... 9

3.2 Rotor Hub ..... 13

3.3 Whole Rotor ..... 14

4. Meshing and Settings ..... 16

4.1 Computational Fluid Domain ..... 16

4.2 Meshing ..... 18

4.3 Settings ..... 24

4.3.1 General Settings ..... 24

4.3.2 Cell Zone Settings and Boundary Conditions ..... 24

4.3.3 Solution Settings ..... 25

5. Results ..... 26

5.1 Convergence of Torque ..... 26

5.2 Characterization of flow field ..... 30

6. Conclusion ..... 45

7. Reference ..... 47

8. Appendices ..... 49

8.1 Appendix A: Details of Meshing ..... 49

8.2 Appendix B: ANSYS Fluent Settings for Problem Setup ..... 52

8.3 Appendix C: ANSYS Fluent Settings for Solution Settings ..... 57

9. Vita ..... 61

# List of Figures

Figure 3.1 Airfoil cross-sections used in the design of the wind turbine rotor blades ..... 11

Figure 3.2 Schematics of the airfoil showing the definition of parameter listed in Table 1 ..... 12

Figure 3.3 Profile of the wind turbine blade..... 12

Figure 3.4 Cross-section of the blade at various RNodes..... 12

Figure 3.5 Schematics of the hub ..... 13

Figure 3.6 The front view of the rotor ..... 14

Figure 3.7 The top view of the rotor ..... 15

Figure 4.1 Computational fluid domain ..... 17

Figure 4.2 Cross sectional view of the fluid domain..... 17

Figure 4.3 Edge sizing on the leading and the trailing edges of the blade ..... 18

Figure 4.4 Edge sizing of the blade tip ..... 19

Figure 4.5 The outer structure of the meshing..... 20

Figure 4.6 The cross-section of the meshing..... 20

Figure 4.7 Mesh in the region near the rotor ..... 21

Figure 4.8 Mesh in the region near the hub..... 21

Figure 4.9 The meshing along the surface of the rotor ..... 22

Figure 4.10 The meshing at the surface of the blade ..... 22

Figure 4.11 The meshing at the tip of the blade ..... 23

Figure 4.12 Mesh quality ..... 23

Figure 5.1 Torque vs. time for the time step size of 0.1s and 0.01s ($\Delta \mathbf{t}$ is time step size)..... 26

Figure 5.2 Torque vs. time with time step size is 0.001s ..... 27

Figure 5.3 Torque vs. time for the time step size of 0.0001s..... 28

Figure 5.4 Torque vs. time for the time step size of 0.00001s..... 28

Figure 5.5 Residuals at various iterations ..... 29

Figure 5.6 Velocity contours of ront view of the computational domain..... 31

Figure 5.7 Velocity contours of back view of the computational domain..... 31

Figure 5.8 Velocity contours at the inlet..... 32

Figure 5.9 Velocity contours at the outlet..... 33

Figure 5.10 Velocity contours at the side surface of the computational domain ..... 33

Figure 5.11 Contour of the rotor and xy-plane at z=0..... 34

Figure 5.12 Velocity contours at z = 0 plane – magnified rotor plane..... 35

Figure 5.13 Velocity contours at z = 0 plane – magnified blade region..... 35

Figure 5.14 Velocity contours at y=0 plane ..... 36

Figure 5.15 Velocity contours at y = 0 plane - magnified near rotor region..... 37

Figure 5.16 Velocity contours at y = 0 plane – magnified blade region..... 37

Figure 5.17 Velocity vectors at z = 100 m, 0 m, -70 m, -150 m and -250 m planes – Front view..... 38

Figure 5.18 Velocity vectors at z = 100 m, 0 m, -70 m, -150 m and -250 m planes – Back view ..... 39

Figure 5.19 Velocity vectors near the rotor region ..... 39

Figure 5.20 Vorticity isosurfaces of 9.7 m/s speed fluid..... 40

Figure 5.21 Vorticity isosurfaces near the rotor region..... 41

Figure 5.22 Static pressure field along the surface of the blade ..... 42

Figure 5.23 Static pressure distribution near the tip of the blade..... 42

Figure 5.24 Wall shear of whole rotor ..... 43

Figure 5.25 The wall shear stress near the tip of the blade ..... 44

Figure 8.1 Edge sizing of the leading and trailing edges of blade ..... 49

Figure 8.2 Edge sizing of blade tips ..... 49

Figure 8.3 Global sizing settings ..... 50

Figure 8.4 Advanced settings ..... 51

Figure 8.5 The outline of the sizing ..... 51

Figure 8.6 General setup ..... 52

Figure 8.7 Viscous model ..... 52

Figure 8.8 Fluid material ..... 53

Figure 8.9 Cell zone settings ..... 53

Figure 8.10 Boundary condition of blade ..... 54

Figure 8.11 Boundary condition of inlet ..... 54

Figure 8.12 Boundary condition of outlet ..... 55

Figure 8.13 Boundary condition of side wall ..... 55

Figure 8.14 The default reference values ..... 56

Figure 8.15 Solution Methods ..... 57

Figure 8.16 Solution Controls ..... 57

Figure 8.17 Monitors ..... 58

Figure 8.18 Residual monitors ..... 58

Figure 8.19 Hybrid initialization ..... 59

Figure 8.20 Calculation activities ..... 59

Figure 8.21 Run calculation ..... 60

# ABSTRACT

Three dimensional transient turbulent flow for the 5 MW wind turbine designed and optimized by National Renewable Energy Lab are characterized. Spatial and temporal characteristics of the flow are examined using ANSYS Fluent commercial software. Turbulent flow structures near and far fields of the rotor region is characterized for the wind speed of 9 m/s and the rotor speed of 1.08 rad/s. The wind turbine is designed using the CATIA CAD software. With the fine mesh used in the rotor region, the number of elements in the mesh used for simulations is 10,640,778. Temporal convergence is attained by using the time step size as small as 0.00001 s. The torque generated by the turbine is 1.806 kNm and the power generation of the turbine is 1.95 MW. The power generated by the wind turbine at the operating condition selected is about 72 % of the maximum potential power that can be generated by any wind turbine at these operating conditions.

# 1. Introduction

In this world, clean energy is booming and becoming more important than any other energy resources. Wind power is a kind of large and inexhaustible resource that has ability to mitigate climate change. Currently, countries in North America and Europe are putting a large amount of investment on the installations of more and more wind farms which have bigger and bigger wind turbines. Since wind energy is the most important avant-garde in developing renewable energy which is so reliable and able to reduce our dependence on fossil fuels, pioneering the research on large-scale wind turbine will reach a milestone.

As we know, there is a long coast of United States which gives a large amount resource of wind energy, especially for offshore wind technology. Since wind increases a lot with long distance on land, then it will generate more electricity along the coast, or even on the shore close to the coast. The National Renewable Energy Laboratory (NREL) estimates that U.S. offshore winds have a gross potential generating capacity four times greater than the nation's present electric capacity [1]. However, this estimation is so conserved that it does not include the sitting constraints and stakeholder inputs. But it still indicates that U.S. has a great capacity of offshore wind resources. In order to optimize the proportion of clean energy in U.S. to 20 % by 2030, National Renewable Energy Lab estimates that the potential 54 GW electricity is able to base on offshore wind turbine.

Although U.S. has this abundant wind resource where is no offshore wind power generating in United States, Europe countries spend lots of investment for the research of offshore wind turbine. In Belgium, to prove the viability of the 5MW offshore wind

turbine after pre-design, the Thortonbank project which is the first phase of the C-Power project has built 6 turbines in Belgian North Sea which are running very well on its test 2009. As a result, the second and third phases of the C-Power project are now ongoing. Meanwhile in the Loire-Atlantique region of France, the biggest offshore wind turbine Alstom's Haliade 150-6MW which has three 73.5 meter blades is being installed from March 2012. Therefore, learning from the work done by European countries will be a good way to support the development of American offshore wind power research.

H.J.T. Kooijman, C. Lindenburg, D. Winkerlaar and E.L. wan del Hooft at Dutch Offshore Wind Energy Convertor (DOWEC) Project have designed a 6MW wind turbine for the Program for Horizontal Axis Turbine Analysis and Simulation (PHATAS) [2]. The wind turbine has a 129m diameter with a 62.7m blade. Researchers at (NREL) have optimized this turbine for 5MW power for offshore applications [3]. The wind turbine used in the present simulations has the design similar to the one optimized by NREL. Further research were conducted to test this concept design and to validate the possibilities of the newly developed computational framework by simulations performed at realistic wind velocity and rotor speed conditions and at full spatial scale [4]. Y. Bazilevs, and M.-C. Hsu have used non-uniform rational B-splines (NURBS) for isogeometric analysis method to simulate one third of the whole rotor which is the reference design of 5 MW wind turbine.

As former research has done a lot on the simulation of this specific turbine, using another more accurate method which is large eddy simulation (LES) is presented in this thesis. However, LES costs a lot CPU time and requires massive parallel computing resources, and LES is not easily applicable to simulate turbulent flows in

complex geometries as in the present study. ANSYS Fluent is employed to conduct flow simulations using a large eddy simulation method with parallel computing which will save a great amount of time, but it requires a powerful computer. And since LES is a time dependent computation, a large amount of storage is needed to save data about the velocity and pressure field at various time steps.

Before running the whole simulation, a clean geometry will be built by CAD software contains lines with sharp angles at the trailing edge generated by those airfoils tips. Since these sharp edged lines will cause plenty of small fragment and sliver in the fluid domain, a short 2 percent incision will be used to avoid these unnecessary small segments. The details of this procedure are presented in chapter 3. Then it needs a good quality of meshing which will be used in this simulation and it will be tested by a general standard offered by ANSYS Meshing. Temporal convergence is tested by calculating torque generated using different time steps. The present results are compared against the results reported by previous investigators examining torque generation. Meanwhile, the contours and isosurfaces of velocity and pressure will be presented to depict the flow field around the rotor and the whole flow field.

# 2. Mathematical Model

## 2.1 Large Eddy Simulation (LES) Model

Large Eddy Simulation presents an idea that using the method of closure of the Reynolds averaged equations for calculation of turbulent flow. From Navier-Stokes equations, the Reynolds equations are filtered by an averaging type where a spatial average is applied to avoid the temporal average. At the same time, these averaged equations which have stress terms must approach to closure by modeling. The equations are then solved in LES are formally developed by "filtering" the Navier-Stokes equations to remove the small spatial scales. The resulting equations describe the evolution of the large eddies and contain the subgrid-scale stress tensor that represents the effects of the unresolved small scales [2].

A filtered variable is defined by [3]

$$\bar{\phi}(x) = \int_D \phi(x') G(x, x')\, dx' \quad (1)$$

where $\phi$ is a space variable whose over-bar variable means a resolved parameter, *D* is the fluid domain and G is the filter function that determines the scale of the resolved eddies.

Meanwhile, Fluent generates filtering result by using finite-volume discretization

$$\bar{\phi}(x) = \frac{1}{V} \int_V \phi(x')\, dx', \quad x' \in V \quad (2)$$

where *V* is the volume of a computational cell. The filter function, $G(x, x')$, is defined by

$$G(x,x') = \begin{cases} \frac{1}{V}, & x' \in V \\ 0, & x' otherwise \end{cases} \quad (3)$$

For incompressible flow simplifying the Navier-Stokes equation yields

$$\frac{\partial \rho}{\partial t} + \frac{\partial}{\partial x_i}(\rho \bar{u}_i) = 0 \quad (4)$$

and

$$\frac{\partial}{\partial t}(\rho \bar{u}_i) + \frac{\partial}{\partial x_j}(\rho \bar{u}_i \bar{u}_j) = \frac{\partial}{\partial x_j}(\sigma_{ij}) - \frac{\partial \bar{p}}{\partial x_i} - \frac{\partial \tau_{ij}}{\partial x_j} \quad (5)$$

where $\sigma_{ij}$ is the stress tensor due to molecular viscosity defined by

$$\sigma_{ij} \equiv \left[\mu\left(\frac{\partial \bar{u}_i}{\partial x_j} + \frac{\partial \bar{u}_j}{\partial x_i}\right)\right] - \frac{2}{3}\mu \frac{\partial \bar{u}_l}{\partial x_l}\delta_{ij} \quad (6)$$

and $\tau_{ij}$ is the subgrid-scale stress defined by

$$\tau_{ij} \equiv \rho\overline{u_i u_j} - \rho \bar{u}_i \bar{u}_j \quad (7)$$

## 2.2 Subgrid-Scale Model

With the filtering operation, the smaller scale stress must be modeled. By using the Boussinesq theory [4] in the models, the subgrid-scale turbulent stresses are generated

$$\tau_{ij} - \frac{1}{3}\tau_{kk}\delta_{ij} = -2\mu_t \bar{S}_{ij} \quad (8)$$

where $\mu_t$ is the subgrid-scale turbulent viscosity. The isotropic part of the subgrid-scale stresses $\tau_{kk}$ is not modeled, but added to the filtered static pressure term. $\bar{S}_{ij}$ is the rate-of-strain tensor for the resolved scale defined by

$$\bar{S}_{ij} \equiv \frac{1}{2}\left(\frac{\partial \bar{u}_i}{\partial x_j} + \frac{\partial \bar{u}_j}{\partial x_i}\right) \quad (9)$$

Then subgrid-scale models which has four main choices [6] including the Smagorinsky-Lilly model, the dynamic Smagorinsky-Lilly model, the WALE (Wall-Adapting Local Eddy-viscosity) model, and the dynamic Kinetic-Energy model in Fluent is used to provide accurate stresses calculations.

The subgrid-scale turbulent flux of a scalar, $\phi$, is modeled using s subgrid-scale turbulent Prandtl number by

$$q_j = -\frac{\mu_t}{\sigma_t}\frac{\partial \phi}{\partial x_j} \quad (10)$$

where $q_j$ is the subgrid-scale flux.

In the present study, the dynamic Smagorinsky-Lilly model is used to generate the result for rotor part of single wind turbine.

The eddy-viscosity of the Smagorinsky-Lilly is defined by

$$\mu_t = \rho L_s^2 |\bar{S}| \quad (11)$$

where $L_s$ is the mixing length for subgrid scales and $|\bar{S}| \equiv \sqrt{2\bar{S}_{ij}\bar{S}_{ij}}$. And $L_s$ is obtained by

$$L_s = min(\kappa d, C_s \Delta) \quad (12)$$

where $\kappa$ is the von Karman constant, $d$ is the distance to the closest wall, $C_s$ is the Smagorinsky constant, and $\Delta$ is the local grid scale. $\Delta$ is computed according to the volume of the computational cell using

$$\Delta = V^{1/3} \quad (13).$$

Lilly [5] derived a value of 0.17 for $C_s$ for homogeneous isotropic turbulence in the inertial subrange. However, this value was found to cause excessive damping of large-scale fluctuations in the presence of mean shear and in transitional flows near solid boundary, and has to be reduced in such regions. In summary, $C_s$ is not a universal constant and is the most serious shortcoming of this simple model. Nonetheless, a $C_s$ value of around 0.1 has been found to yield the best results for a wide range of flows, and is the default value in ANSYS Fluent.

The Smagorinsky model constant $C_s$ is dynamically computed based on the information provided by the resolved scales of motion. Thus $C_s$ is dependent on the local mesh size since this is the primary factor in calculation of the local filtering characteristics. Fluent clips $C_s$ at zero and 0.23 in order to maintain numerical stability in the iteration process. [5]

# 3. Wind Turbine Rotor

After comparing different kinds of wind turbines, the NREL offshore 5 MW baseline wind turbine emerges from several articles and reports. This large scale offshore wind turbine has progressed on second and third phases of C-Power project in Belgian North that includes six 5 MW wind turbines. It is possible that the predictions obtained from current work can be compared to the results produced by these studies. And since the DOWEC 6 MW pre-design [6] has been well modified and further improved by the DOWEC project, the design of 5 MW wind turbine has a reliable result offered by former research by Jonkman [7].

## 3.1 Rotor Blade

The blade of the rotor is based on the 5 MW offshore baseline wind turbine offered by Jonkman. And the blade geometry data taken from the reference are summarized in Table 1 [8]. The root part of the blade is a perfect cylinder. But there is some optimization applied compared with previous research. Earlier investigators used blades having an abrupt transition from cylinder to DU (Delft University) 40 airfoil. Such abrupt transitions make the geometry not smooth and lead to erroneous stress distribution along the blades. A linear relationship between the location of aerodynamic center and horizontal and vertical chords is used to obtain a smoother transition

$$y = k \cdot x + b \quad (14)$$

where y = 0.5 to 0.25 is the location of aerodynamic center, and x = 1 to 1/7 is the proportion.

In equation (14) k and b are calculated to be 7/24 and 5/24, respectively. Equation (14) becomes,

$$y = \frac{7}{24}x + \frac{5}{24} \quad (15)$$

Thus when y = 0.44, x = 0.7943, the length of the minor axis is 3.0612 m and when y = 0.38, x = 0.5886, the length of the minor axis is 2.4527 m.

**Table 1. Wind turbine rotor geometry definition**

| RNodes(m) | AeroTwst(deg.) | Chord(m) | AeroCent(-) | AeroOrig(-) | Airfoil(-) | TwistAxis |
|---|---|---|---|---|---|---|
| 2 | 13.308 | 3.542 | 0.25 | 0.5 | Cylinder | 0.5 |
| 2.8667 | 13.308 | 3.542 | 0.25 | 0.5 | Cylinder | 0.5 |
| 5.6 | 13.308 | 3.854/ 3.0612 | 0.2218 | 0.44 | Ellipse | 0.4682 |
| 8.3333 | 13.308 | 4.167/ 2.4527 | 0.1883 | 0.38 | Ellipse | 0.4417 |
| 11.75 | 13.308 | 4.557 | 0.1465 | 0.3 | DU40 | 0.4035 |
| 15.85 | 11.48 | 4.652 | 0.125 | 0.25 | DU35 | 0.375 |
| 19.95 | 10.162 | 4.458 | 0.125 | 0.25 | DU35 | 0.375 |
| 24.05 | 9.011 | 4.249 | 0.125 | 0.25 | DU30 | 0.375 |
| 28.15 | 7.795 | 4.007 | 0.125 | 0.25 | DU25 | 0.375 |
| 32.25 | 6.544 | 3.748 | 0.125 | 0.25 | DU25 | 0.375 |
| 36.35 | 5.361 | 3.502 | 0.125 | 0.25 | DU21 | 0.375 |
| 40.45 | 4.188 | 3.256 | 0.125 | 0.25 | DU21 | 0.375 |
| 44.55 | 3.125 | 3.01 | 0.125 | 0.25 | NACA64 | 0.375 |
| 48.65 | 2.319 | 2.764 | 0.125 | 0.25 | NACA64 | 0.375 |
| 52.75 | 1.526 | 2.518 | 0.125 | 0.25 | NACA64 | 0.375 |
| 56.1667 | 0.863 | 2.313 | 0.125 | 0.25 | NACA64 | 0.375 |
| 58.9 | 0.37 | 2.086 | 0.125 | 0.25 | NACA64 | 0.375 |
| 61.6333 | 0.106 | 1.419 | 0.125 | 0.25 | NACA64 | 0.375 |
| 62.9 | 0 | 0.7 | 0.125 | 0.25 | NACA64 | 0.375 |

After gradual diminution of the chord, NACA 64 profile is used all along to the blade tip. The blade is based on the specification listed in the column of airfoil. Airfoil profiles are depicted in Figure 3.1.

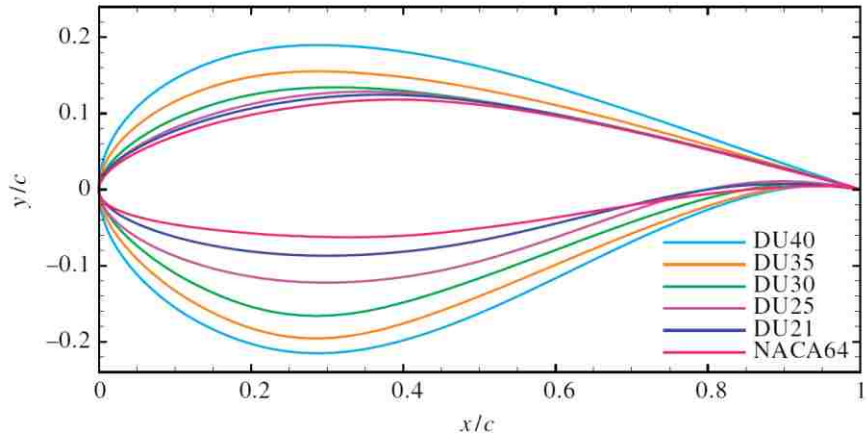


**Figure 3.1 Airfoil cross-sections used in the design of the wind turbine rotor blades**

The ‘RNodes’ listed in Table 1 represent the length between the origin and the position of the specific airfoil along the direction of the blade axis. The ‘AeroTwist’ shows the angle between the horizon and chord. Airfoils in different cross-sections are twisted to improve the quality of aerodynamics of this blade when it is incorporated in rotor. The ‘Chord’ denotes the chord length of the airfoil, and the ‘AeroOrig’ shows the location of the aerodynamic center. ‘TwistAxis’ = ‘AeroOrig’ + (0.25 – ‘AeroCent’) represents the fractional location of where the blade-picth axis passes through each airfoil cross-section. The relationship between ‘AeroOrig’, ‘Areotwist’, ‘Bland-pitch’ and ‘AeroCent’ is shown in Figure 3.2 [8].

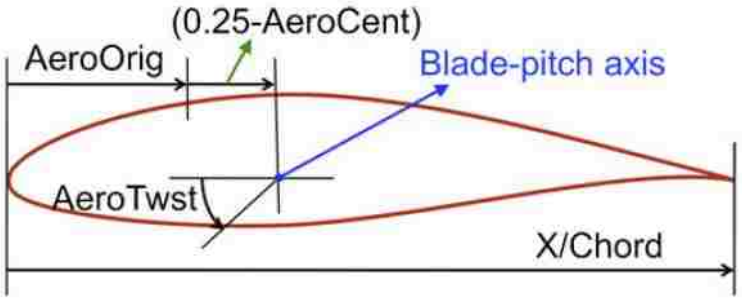


**Figure 3.2 Schematics of the airfoil showing the definition of parameter listed in Table 1**

The wind turbine blade is designed using CATIA which is a commercial software. The profile of the single wind turbine blade is shown in figure 3.3 while the cross-sections of the blade at various RNodes are depicted in in figure 3.4.

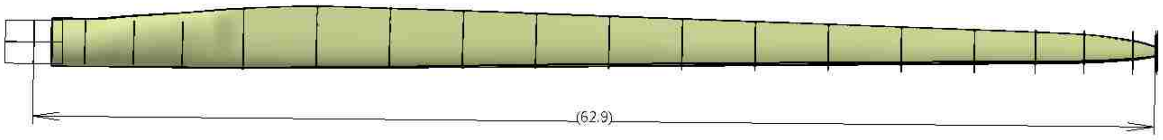


**Figure 3.3 Profile of the wind turbine blade**

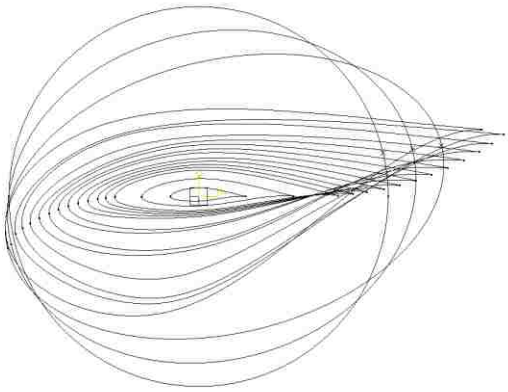

**Figure 3.4 Cross-section of the blade at various RNodes**

## 3.2 Rotor Hub

As the hub is the main supporting part of the three blades, there is not much information in the literature to show the exact structure of this rotor hub. The present work introduces a new design that is used in the computational fluid dynamics simulation. Since the area of hub is very small compared with the whole rotating area, it will not affect the accuracy of the simulation conducted with the well designed blades.

Figure 3.5 shows the semi-cross section of the rotor hub along the z direction. The spline is used with the four points labeled in the graph to design the hub, shown in figure 3.5.

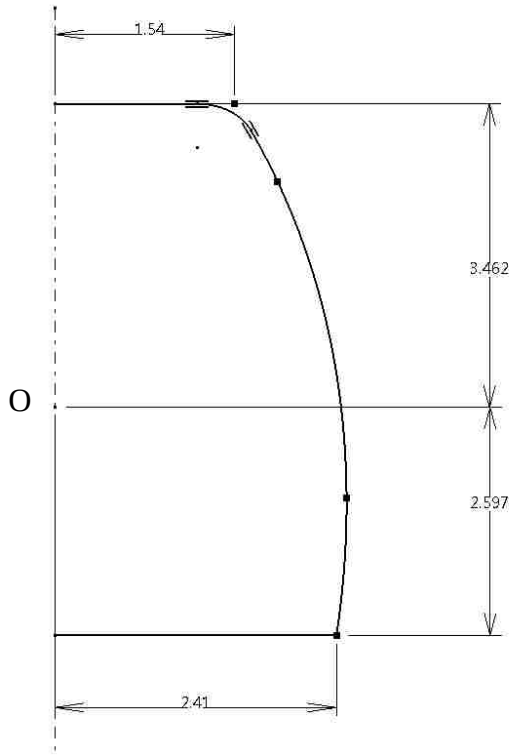


**Figure 3.5 Schematics of the hub**

As it is shown in the sketch, the area of the hub facing z-direction is 18.24 $m^2$, while the rotating area of the whole rotor is 12,423 $m^2$. The percentage of the hub area to

the rotating area is 1.47 %. The area of the computational domain is three times larger than the rotating are. Hence, the influence of the hub on the flow field is not expected to be significant.

## 3.3 Whole Rotor

The rotor consists of the blades and the hub. Front and top vies of the rotor are shown in figure 3.6 and 3.7.

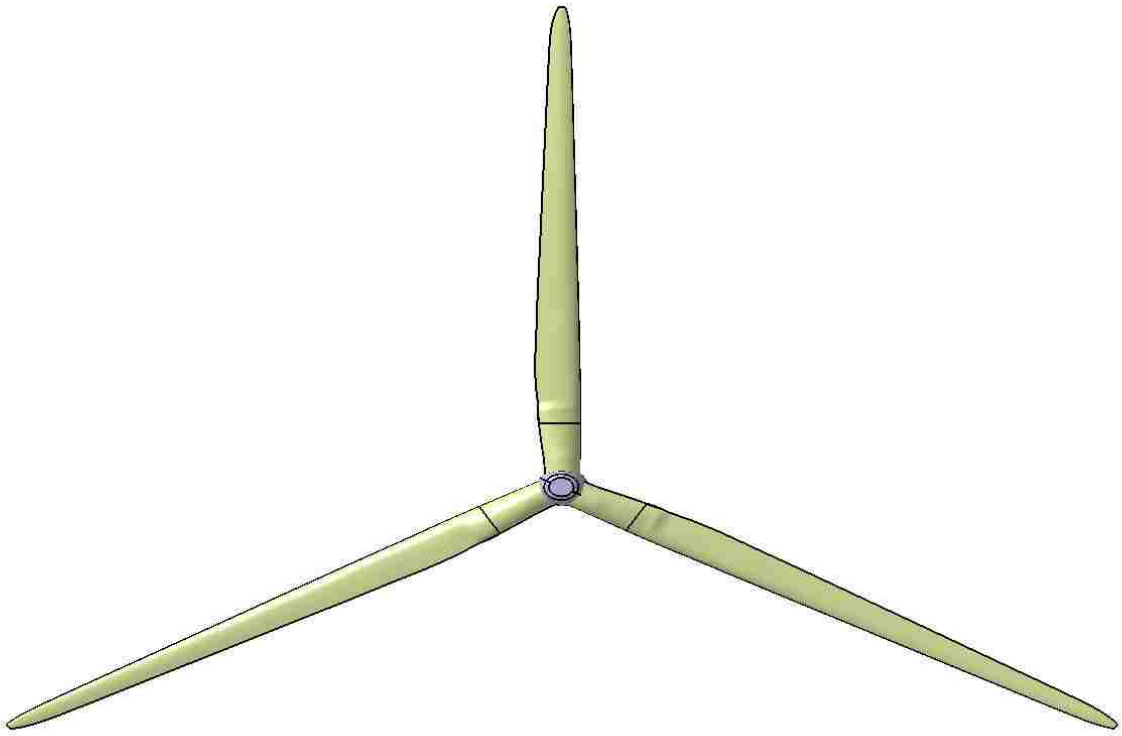

**Figure 3.6 The front view of the rotor**

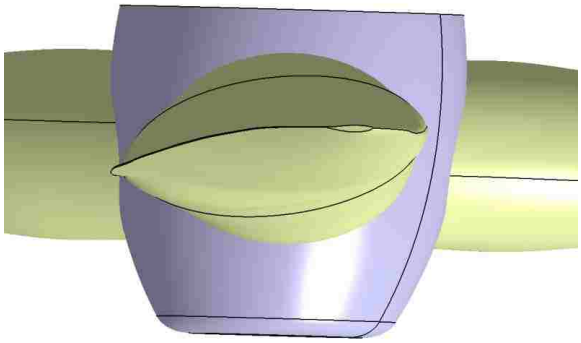

**Figure 3.7 The top view of the rotor**

It is noted that, the blade has been incised two percent of every airfoil to avoid sharp sliver or other cracks to avoid broken meshes. Hence, the trailing edge of the blade is not sharp point but is a plane.

# 4. Meshing and Settings

## 4.1 Computational Fluid Domain

The wind turbine includes rotor, nacelle, tower and foundation. Since the effect of the tower on the flow field is negligible, CFD simulations are conducted by considering only the rotor. The far field boundary conditions are applied on the surface of the cylinder, as shown in the figure 4.1. Computational fluid domain contains the rotor region as a small cylinder of 63 m radius. The computational fluid domain is denoted by the outer cylinder of 200m in radius. The cross-section of the computational domain is shown in figure 4.2. The upstream of the rotor region is 100 m long while the downstream of the rotor is 250 m long.

The use of the small inner cylinder as a rotor region has no significance for the application of boundary conditions. It is simply used for the body of influence for the meshing. Body of influence is a sizing option that allows user to refine a mesh by defining one body as a size source for another body. The body of influence affects the mesh density of the body to which it is scoped, but it will not be meshed [3].

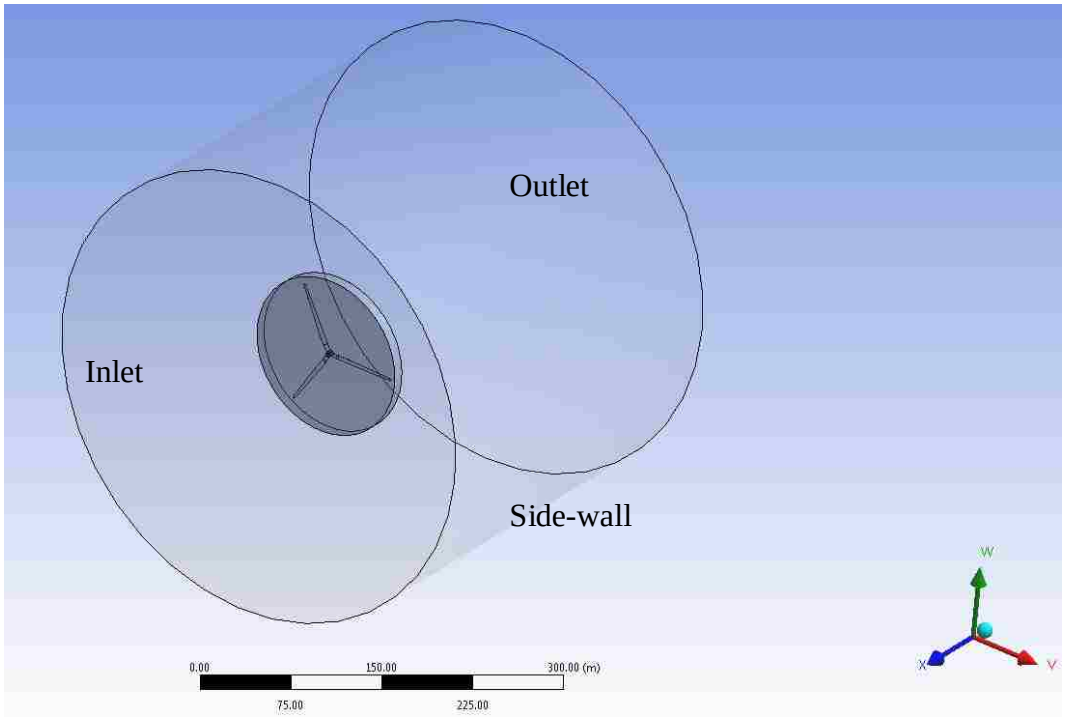


**Figure 4.1 Computational fluid domain**

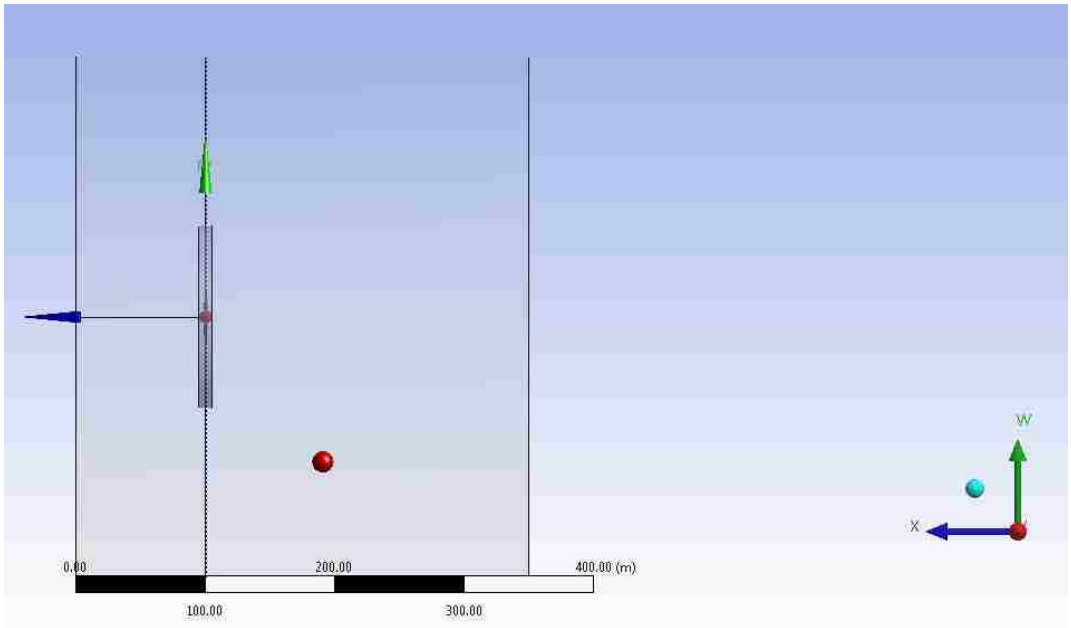


**Figure 4.2 Cross sectional view of the fluid domain**

## 4.2 Meshing

It is critical to have a well defined meshing for successful computational fluid dynamics simulations. For torque, the focus is on the blades of the rotor, there must do refined meshing in the region near the. The entire computational domain is so large that if we do fine meshing in the whole region, it will make the number of elements too large, and lead to a longer computational time and a greater demand for computational resources. Therefore, to have some coarse mesh behind the rotor will give a large decrease on the number of elements and nodes and speed up the calculation time.

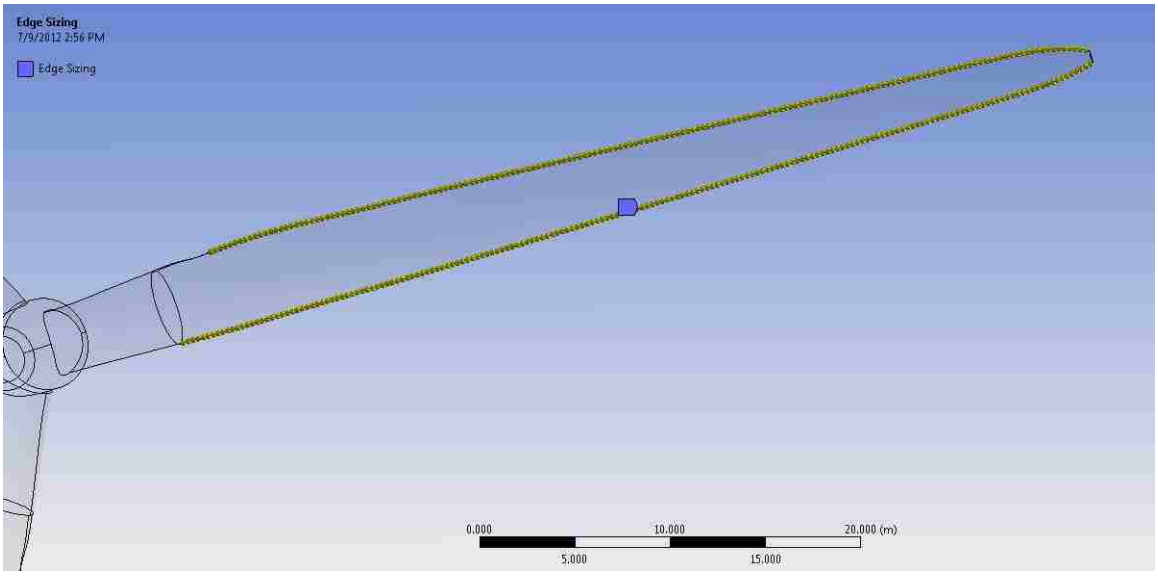


**Figure 4.3 Edge sizing on the leading and the trailing edges of the blade**

Edge sizing is used to obtain more accurate meshing. Figure 4.3 shows 9 edge settings as 0.3m for every element with no bias. Since vortex is typically generated at the blade tip, high quality mesh along the tips is needed. There are also 9 edges for the 3 blade tips with 0.03 m for element length and bias factor of 5. Another type of edge sizing is shown in figure 4.4. The details of the meshing are described in Appendix A.

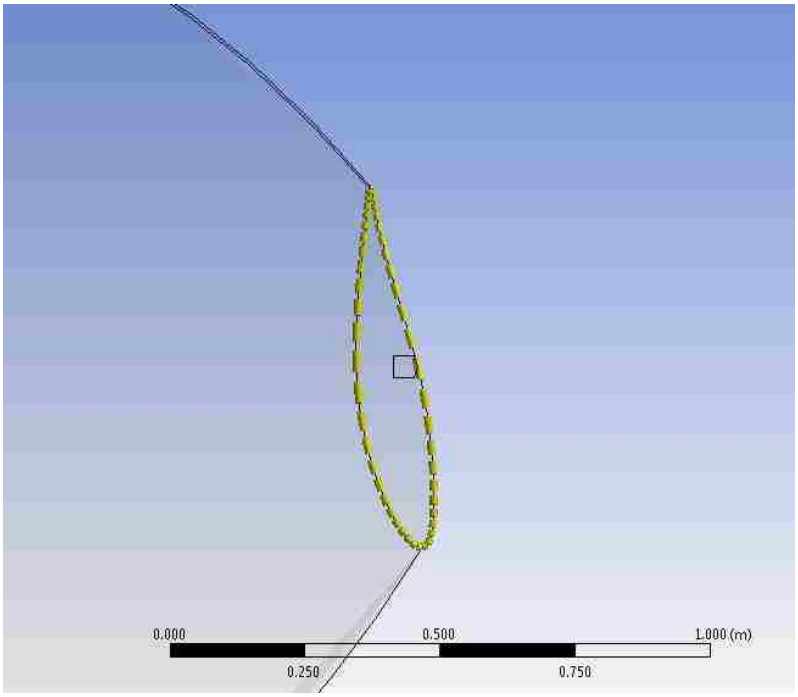


**Figure 4.4 Edge sizing of the blade tip**

In order to size the ANSYS Meshing, advanced size function is employed for the proximity and the curvature. The relevance center is set to be fine and smoothing is set to be medium. The minimum size of the element size is 0.03 m, and the max size is 19.4220 m. The other settings are default which is shown in Appendix A. For inflation around the blade, there are 5 layers with the growth rate of 1.2, and a smooth transition. The inflation area also includes the side-wall and the outlet. Figure 4.5 shows the outer structure of the meshing, while the figure 4.6 shows the cross-section of the generated mesh.

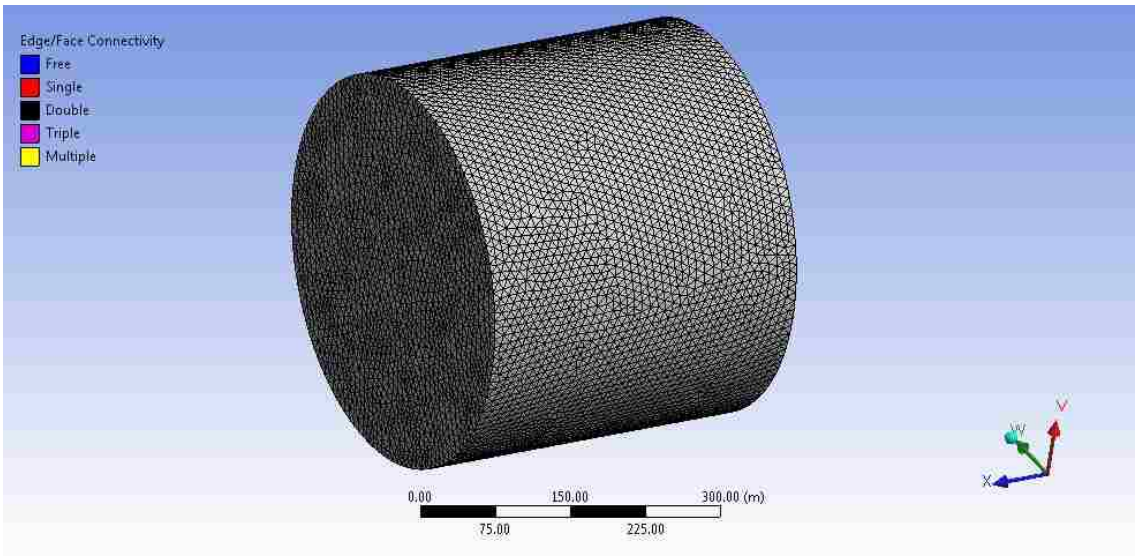


**Figure 4.5 The outer structure of the meshing**

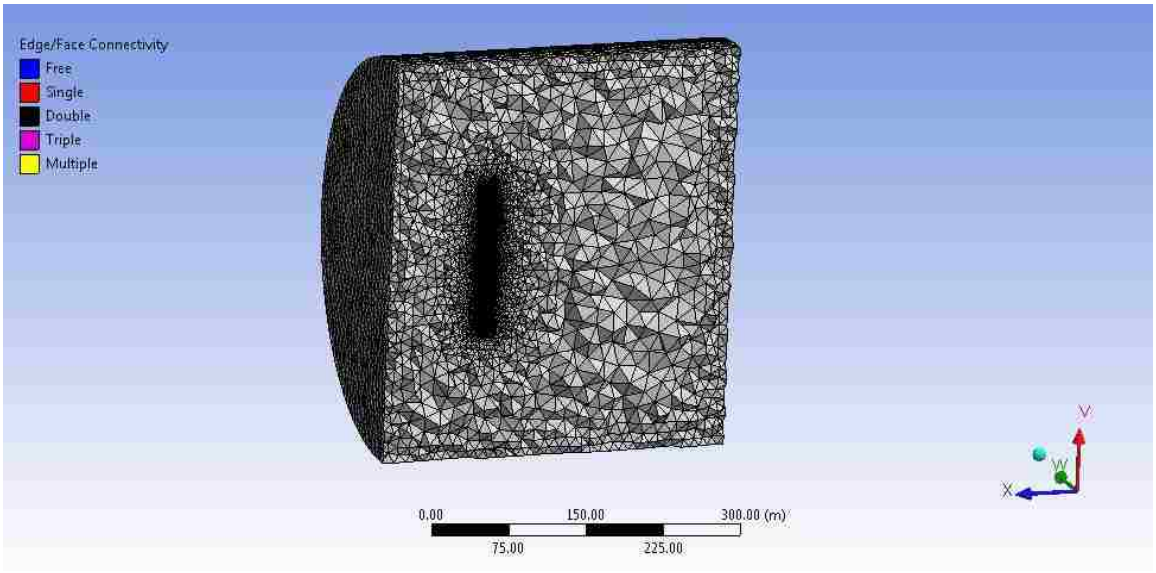


**Figure 4.6 The cross-section of the meshing**

The computational fluid domain has 2,322,690 nodes and 10,640,778 elements. In order to show the detailed structure of the meshing in the rotor region, the magnified images of the mesh is shown in the figures 4.7 and 4.8. The detailed distribution of the tetrahedrons and wedges are clearly seen in these figures.

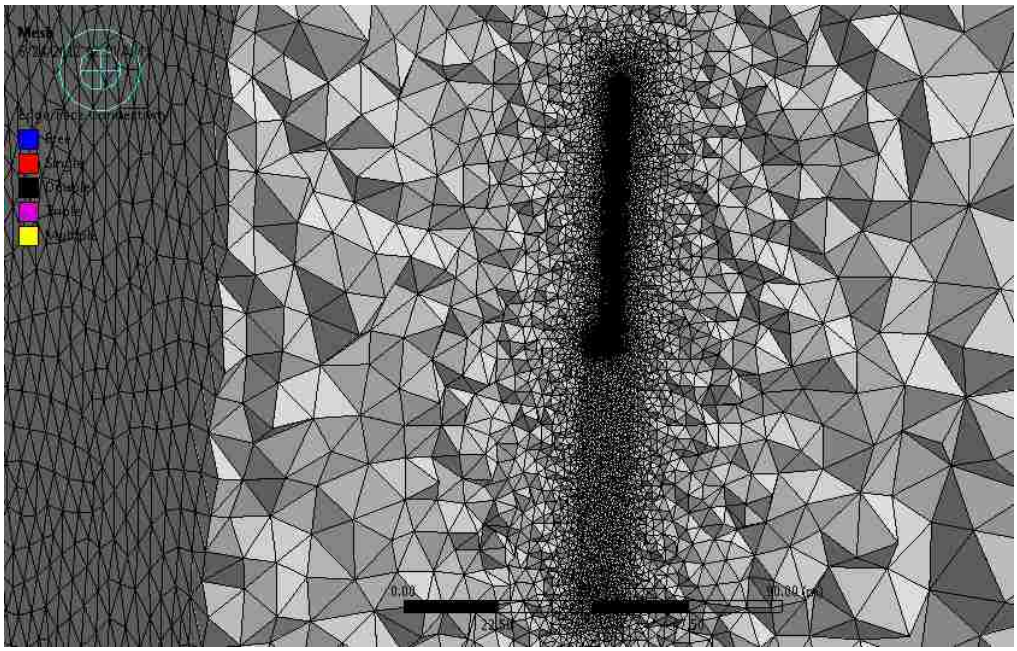


**Figure 4.7 Mesh in the region near the rotor**

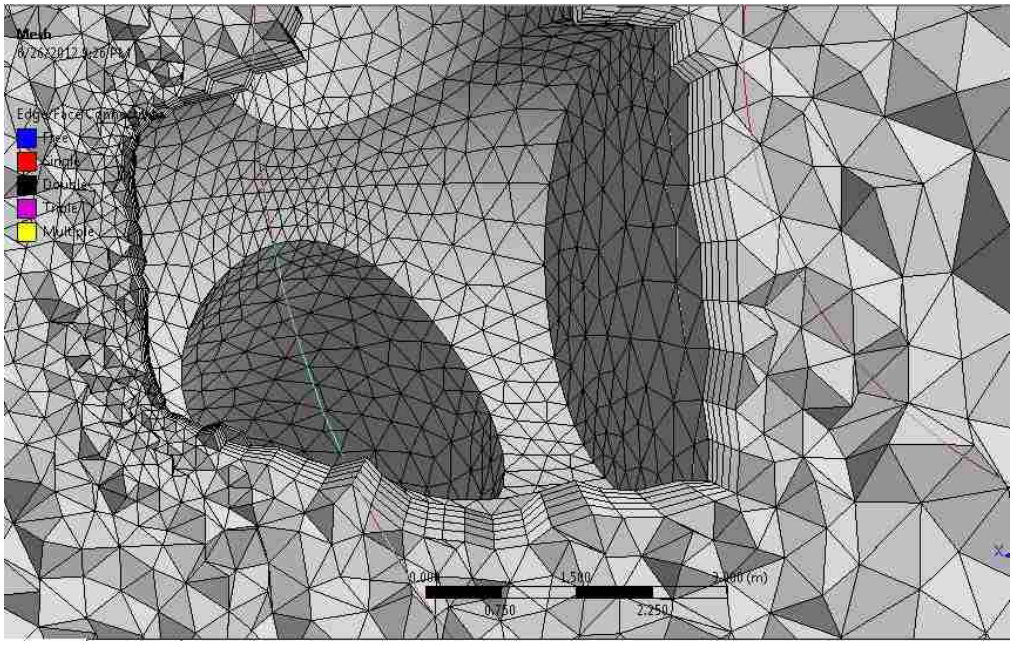


**Figure 4.8 Mesh in the region near the hub**

Figure 4.9, 4.10 and 4.11 show the meshing at the surface of blades. Figure 4.9 show meshing in all three blades while figure 4.10 illustrates the expanded version of the meshing over one blade. Figure 4.11 shows the details of the mesh at the tip of the blade.

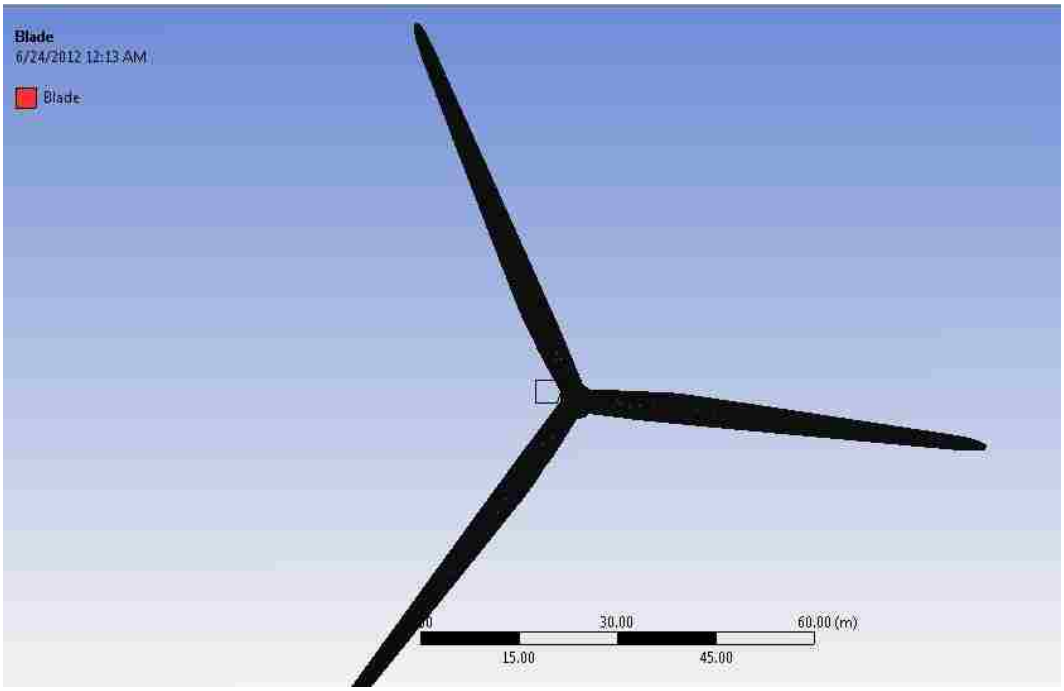


**Figure 4.9 The meshing along the surface of the rotor**

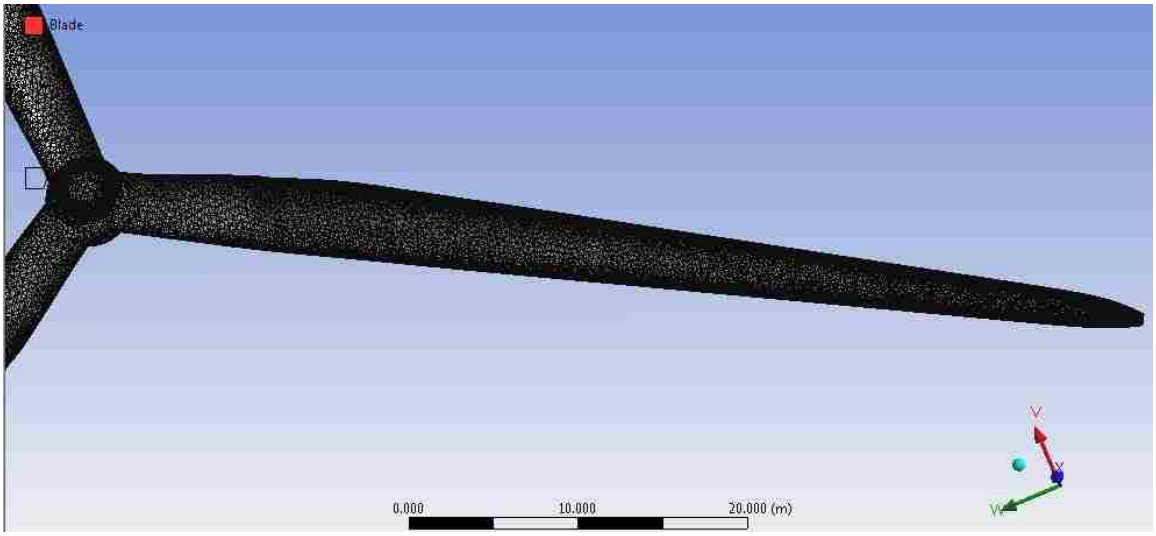


**Figure 4.10 The meshing at the surface of the blade**

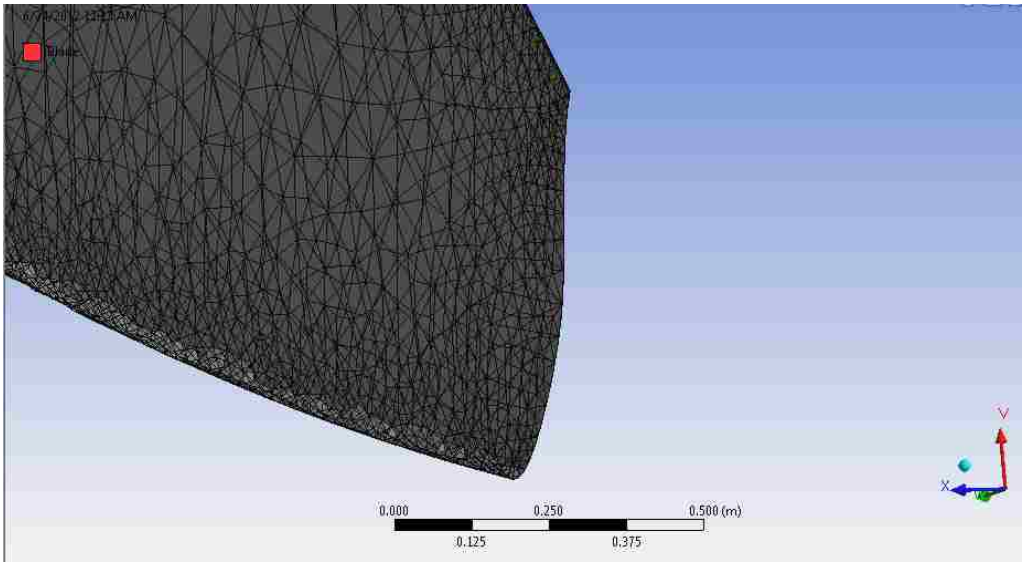


**Figure 4.11 The meshing at the tip of the blade**

After meshing for the entire flow domain, the mesh quality is to be checked. Skewness is calculated for the mesh, and the maximum skewness value of the mesh is calculated as 0.898378, that is less than 0.95 as shown in figure 4.12. So the quality is acceptable for the flow simulations.

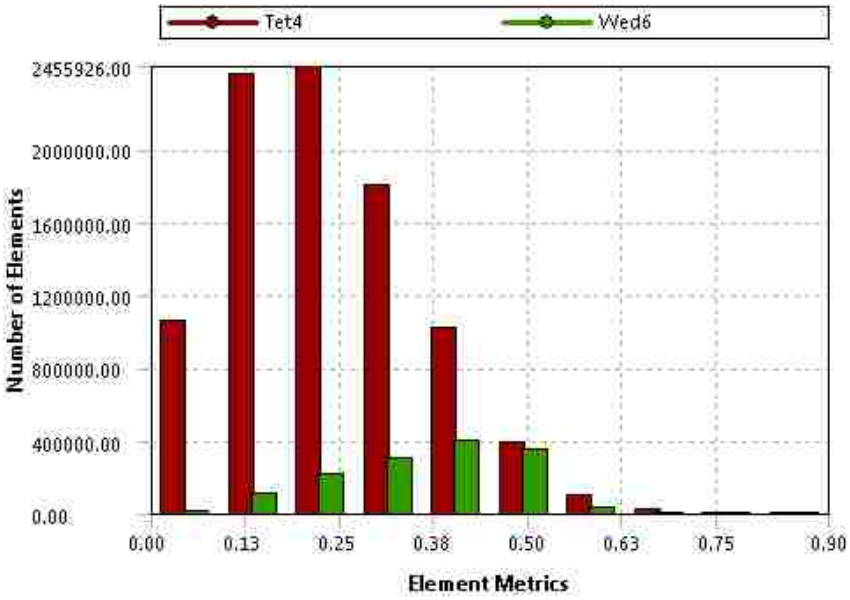


**Figure 4.12 Mesh quality**

## 4.3 Settings

Setting for CFD simulations is done using workbench. The transient 3D simulations for the computational domain described at the previous section request to employ parallel programming which is described in the Appendices B and C. The details of ANSYS Fluent settings for the flow simulations conducted here is described in the Appendices B and C.

### 4.3.1 General Settings

For successful CFD simulations the solver method and the model have to be specified. Large eddy simulation model is used to perform the transient flow simulations. The model is based on pressure and absolute velocity formulation. The pressure-based solver is recommended for incompressible flow, and the absolute velocity formulation is the result of incoming uniform flow. And as mentioned above, the dynamic Smagorinsky-Lilly model is used for sub-scale grid. The flowing fluid is air with a constant density of 1.225 $\mathrm{kg/m^3}$ and viscosity of $1.7894 \times 10^{-5}$ $\mathrm{kg/(m \cdot s)}$.

### 4.3.2 Cell Zone Settings and Boundary Conditions

Equations governing the fluid motion in the frame rotating with the rotor are solved. In this frame of reference, the rotor is stationary while the fluid and the outer boundaries are rotating. The frame motion is set with the angular the speed of -1.08 rad/s rotating along the z-axis relative to the cell zone.

The cylindrical shaped computational fluid domain has four main boundaries. First, the blade has a moving wall relative to adjacent cell zone with the rotational speed

of 0 - no-slip boundary condition. Second, at the inlet uniform axial flow with fluid speed of -9 m/s is imposed. Third, at the outlet zero pressure boundary condition is applied. Finally, the side wall is a moving wall with an absolute rotating speed of 0 rad/s. Shear stresses in the direction of x, y and z are taken as $1 \times 10^{-5}$ pascal.

### 4.3.3 Solution Settings

For the size of mesh used in the present numerical simulations, it is proper to use SIMPLE, pressure-based solver, as indicated in the Appendix C. The spatial discretization employs Green-Gauss cell based gradient, the standard pressure and the bounded central differencing momentum, while it uses the first order implicit transient formulation. For the under-relaxation factors, the pressure factor is 0.3, the density factor is 1, the body forces factor is 1, and the momentum factor is 0.7. But if the solution diverges, the under-relaxation factors needs to be reduced. At the same time, the convergence tolerance on the continuity, x-, y- and z-momentum equations is set to be $1 \times 10^{-6}$. Since the meshing has a complex topology, hybrid initialization is used to generate better initial guess for the velocity and the pressure fields. That helps to accelerate to attain converged solution. The maximum iteration is selected to be 30 at the beginning of the simulation and the time step size is 0.1 s. However, much smaller time step size such as 0.01 s, 0.001 s and 0.0001 s are used to improve the accuracy of the simulation. For all numerical runs the larger fine steps is used to initialize the simulation and the final results are produced using much smaller time steps.

# 5. Results

For the computational fluid dynamics simulation presented here, a uniform velocity of 9 m/s is considered at the inlet. The rotor speed is set to 1.08 rad/s. Hinze [7] reported that at these wind conditions and rotor speed, blade pitching does not take place and the rotor develops a favorable aerodynamic torque of 2,500 kNm [8]. The objective of the present work is to attain the maximum torque of 2,500 kNm and to prove that the meshing and the methods employed here can be used to character the temporal and spatial natures of the flow near and far field of the rotor.

## 5.1 Convergence of Torque

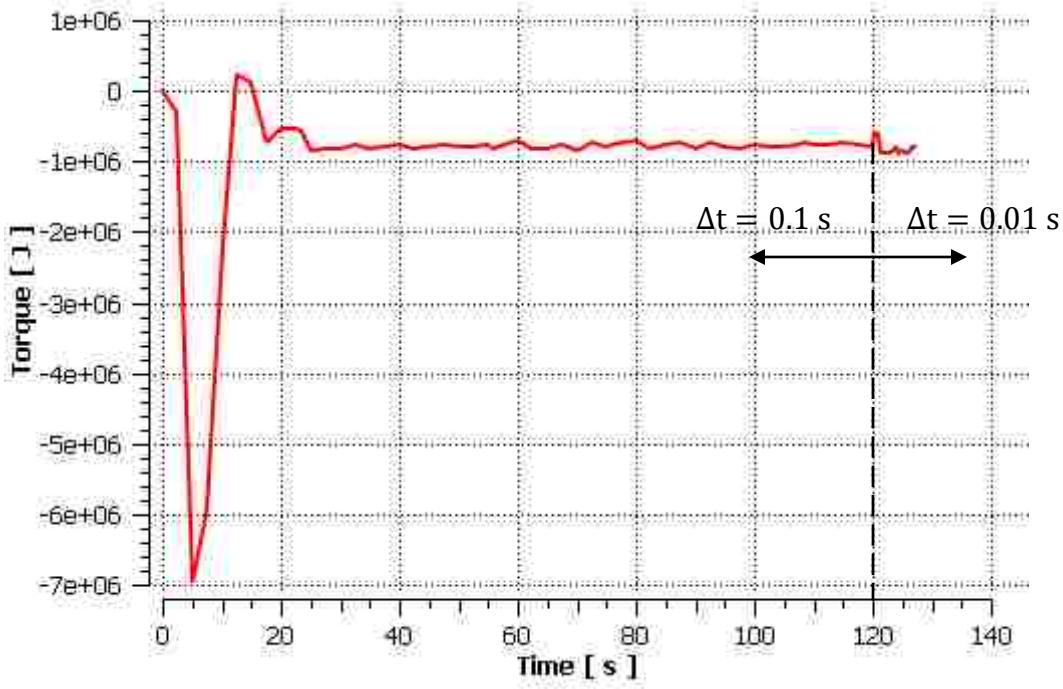


**Figure 5.1 Torque vs. time for the time step size of 0.1 s and 0.01 s (Δt is time step size)**

The early stage of the simulation obtained using the time step of 0.1 s is shown in figure 5.1 as the torque generated by the wind turbine as a function of time. After the transient response from the system, the torque tends to the steady state value of 798.92 kNm with a very small fluctuation, as shown in the left part of figure 5.1. Next, the step is reduced to 0.01 s and after 700 time steps, at t = 127 s, the torque reaches a steady state value of 787.69 kNm, as shown in the right part of figure 5.1.

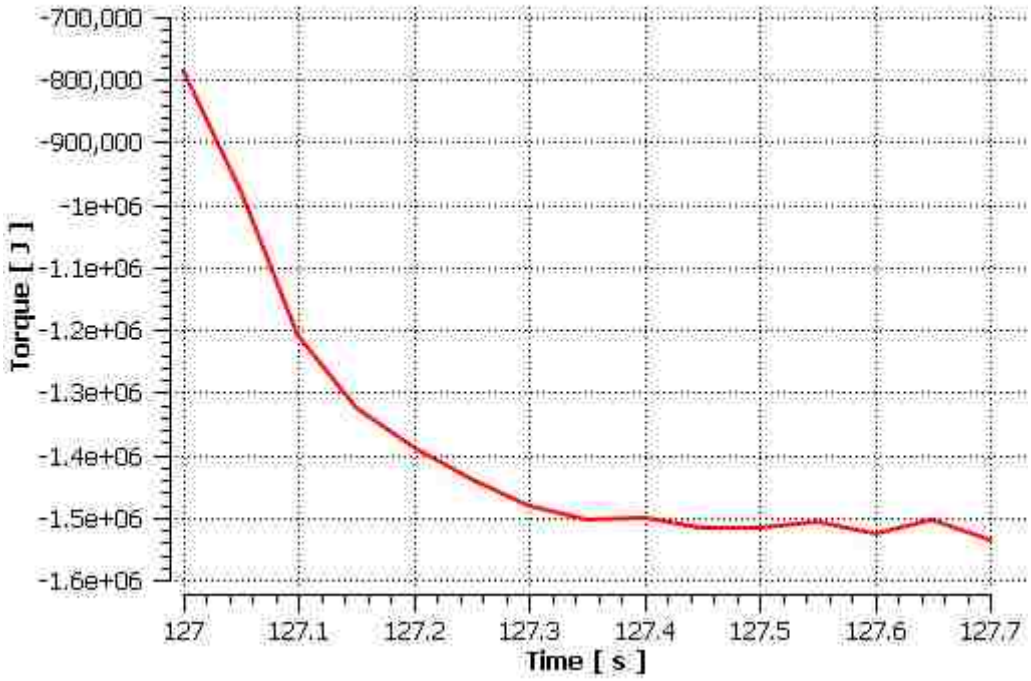


**Figure 5.2 Torque vs. time with time step size is 0.001 s**

Another 700 time steps are simulated with the step size of 0.001 s. The steady state value of the torque has reached to 1,536 kNm, as shown in figure 5.2.

The steady state value of the flow parameters obtained using the time step size of 0.001 s is used as an initial guess for the simulations conducted with the time step size of 0.0001 s. The steady state value of torque is calculated to be 1,832 kNm at t = 128.525 s after 15,250 time steps.

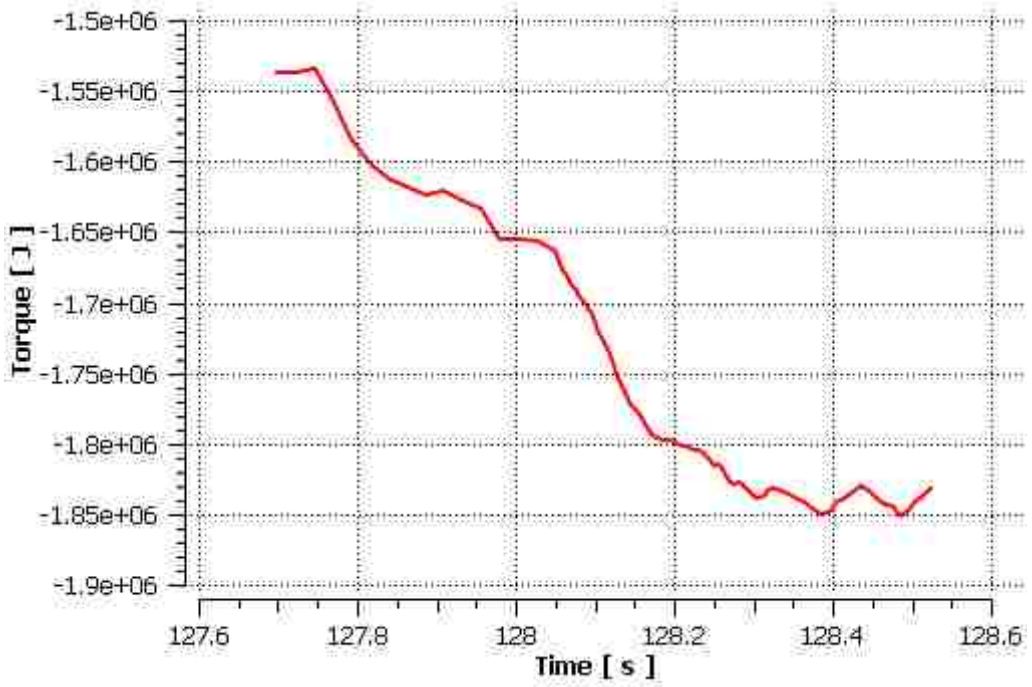


**Figure 5.3 Torque vs. time for the time step size of 0.0001 s**

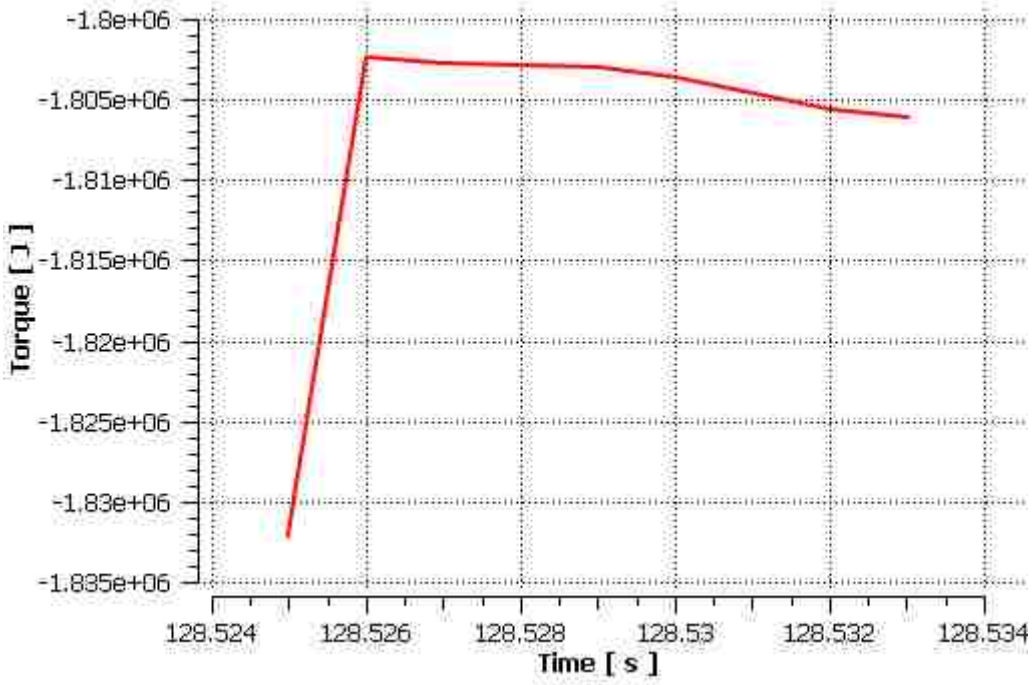


**Figure 5.4 Torque vs. time for the time step size of 0.00001 s**

With the smallest time step size of 0.00001 s the torque is settled around 1,806 kNm, as shown in figure 5.4.

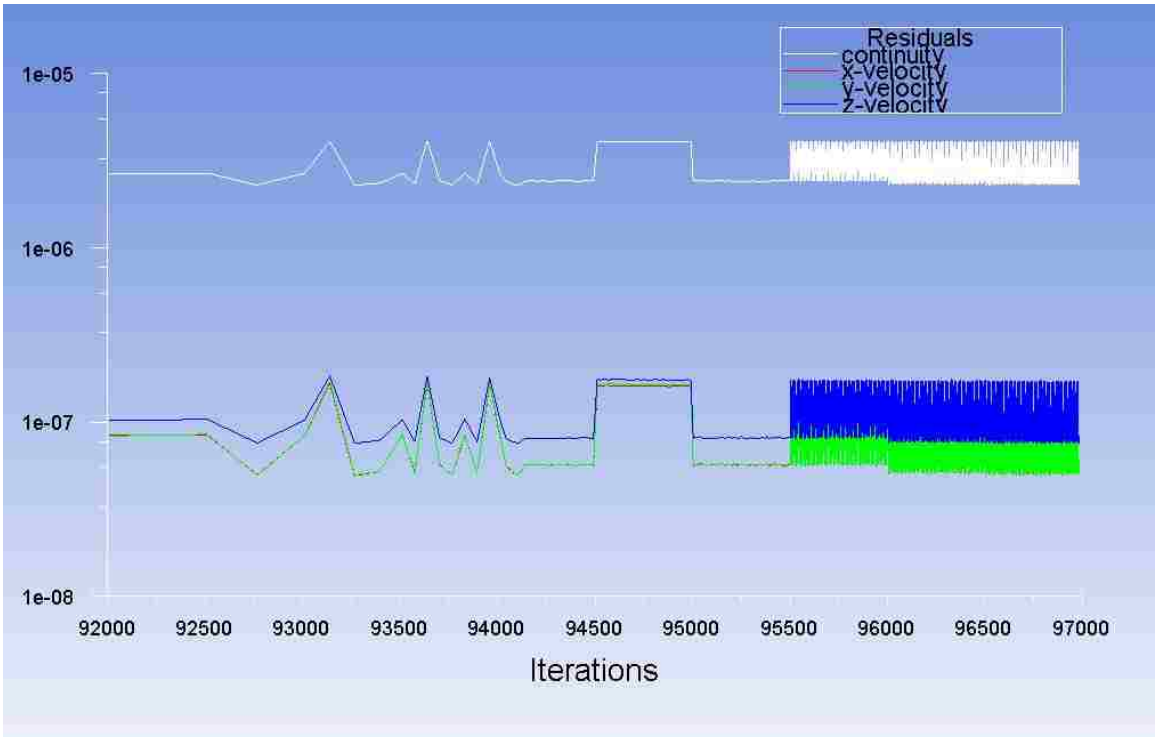


**Figure 5.5 Residuals at various iterations**

The residual of continuity equation reaches around $2.5 \times 10^{-6}$, while the residuals of equations of x-, y- and z-components of the moment equations reach around $1.0 \times 10^{-7}$. This level of tolerance is considered to be sufficient for large scale complex flow simulation.

The power generated by the wind turbine can be determined using the calculated aerodynamic torque and the rotor speed,

$$P = T_f w = 1{,}806.14\ kNm * 1.08\ rad/s = 1.95\ MW.$$

The maximum potential power is determined from the maximum potential toque as [3],

$$P_0 = T_{f0} w = 2{,}500\ kNm * 1.08\ rad/s = 2.70\ MW.$$

The wind turbine aerodynamic torque efficiency is calculated to be,

$$\eta = \frac{P}{P_0} = \frac{1.95}{2.70} \times 100\% = 72.2\%.$$

Meanwhile, this accuracy is more reasonable compared with the general case which is 56.8% [8] for LES transient case.

## 5.2 Characterization of flow field

Front and back vies of the three dimensional flow field are shown in figure 5.5 and 5.6 as the velocity contours in the whole computational flow domain. Red color denotes the high speed region while dark blue color represents the region with low fluid speed. The maximum fluid speed is calculated to be 115.3 m/s.

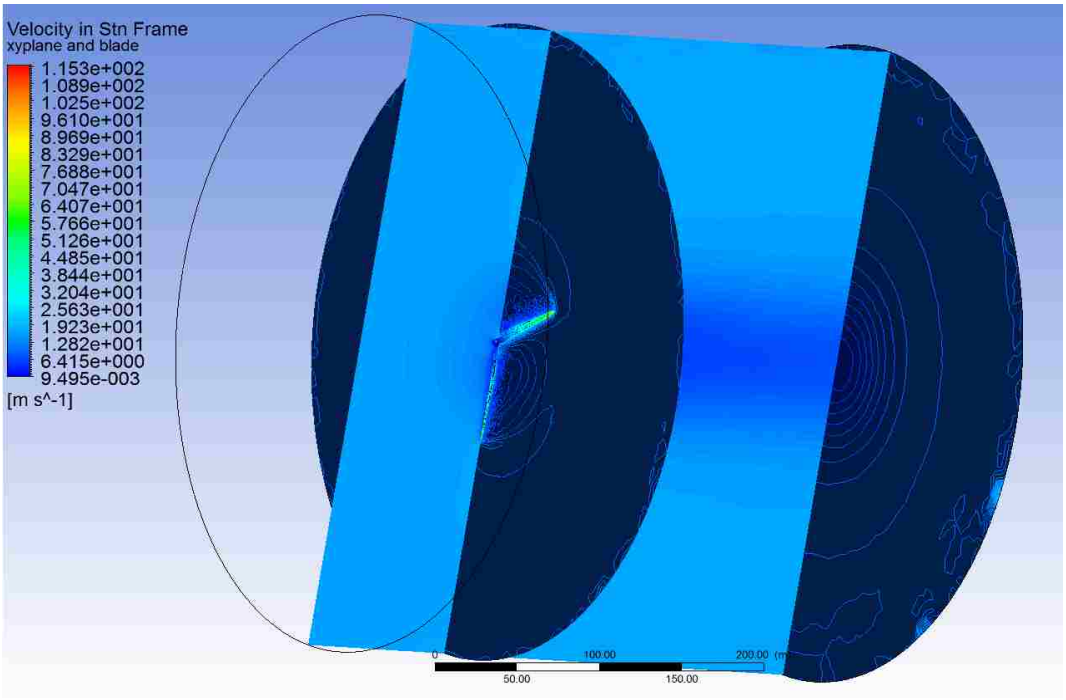


**Figure 5.6 Velocity contours of ront view of the computational domain**

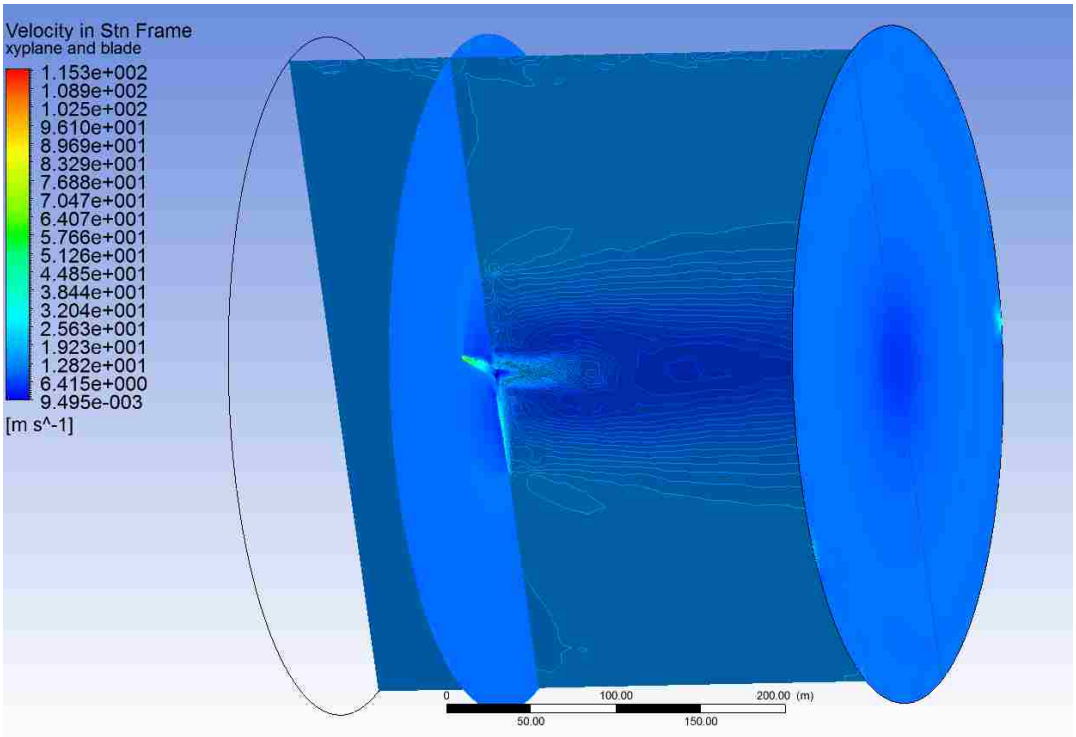


**Figure 5.7 Velocity contours of back view of the computational domain**

Figure 5.8 shows the velocity contour at the inlet at t = 128.525 s. As expected, nearly uniform fluid speed at 9 m/s is observed.

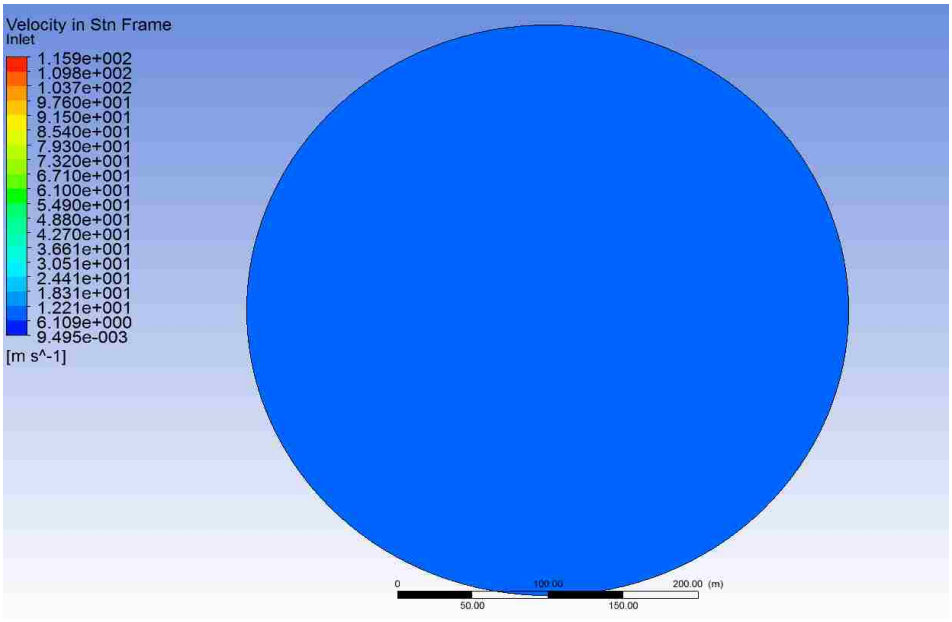


**Figure 5.8 Velocity contours at the inlet**

Figure 5.9 depicts the velocity contours at the outlet. The fully developed turbulent flow is reached at the wake of the rotor. It clearly indicates that the inner flow gradually approaches to the flow in the free stream. There are small levels of flaws around the edges of the cylindrical flow domain caused by the pressure difference between the side wall and the outlet. That is acceptable for highly turbulent flow simulated in large fluid domain. The flow field at the side surface of the flow domain structures with the maximum flow speed of 9 – 10 m/s.

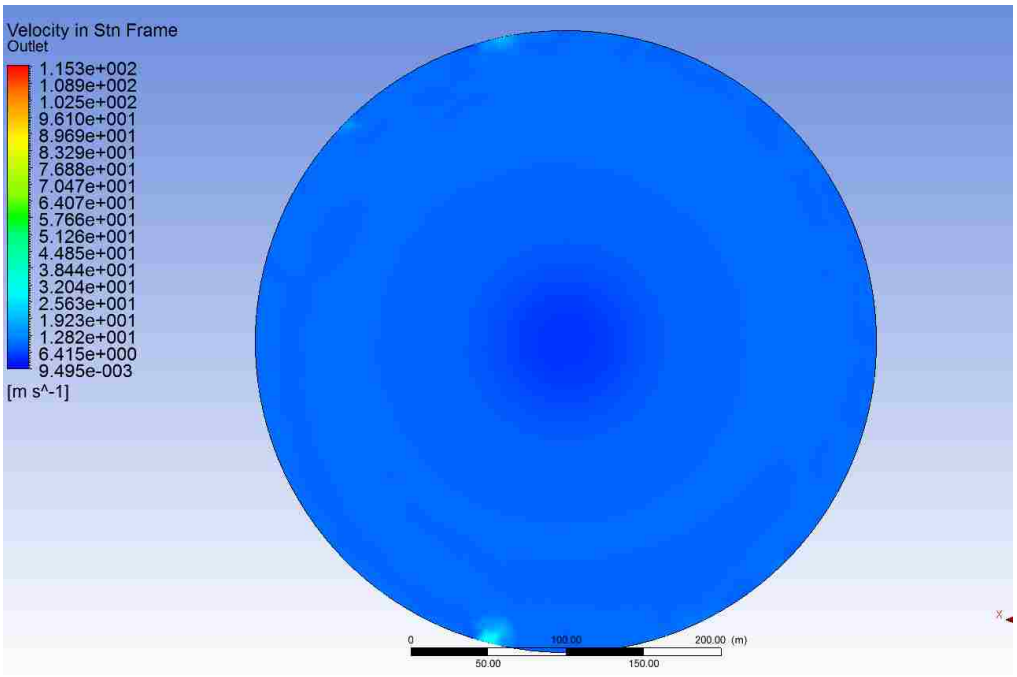


**Figure 5.9 Velocity contours at the outlet**

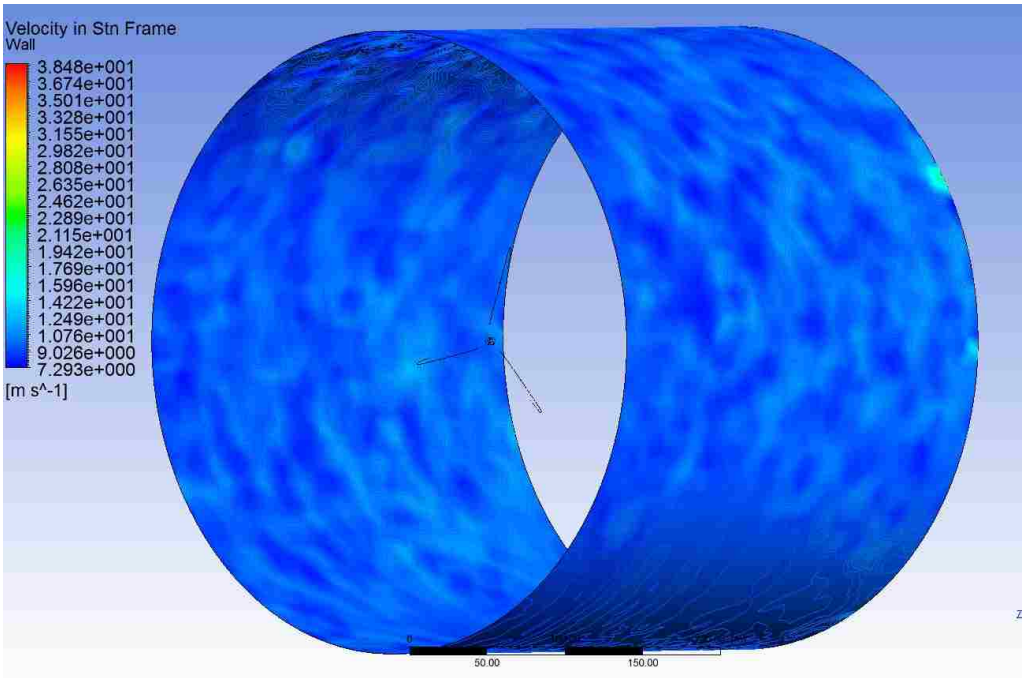


**Figure 5.10 Velocity contours at the side surface of the computational domain**

The velocity contours at the rotor plane ( xy-plane at z = 0 ) are shown in figure 5.11. Velocity contours in the region around the rotor and a single blade are shown in figures 5.12 and 5.13 as magnified images. The rotor is rotating in the clockwise direction. The turbulent flow structures are clearly seen in the region near the trailing edge of the blades.

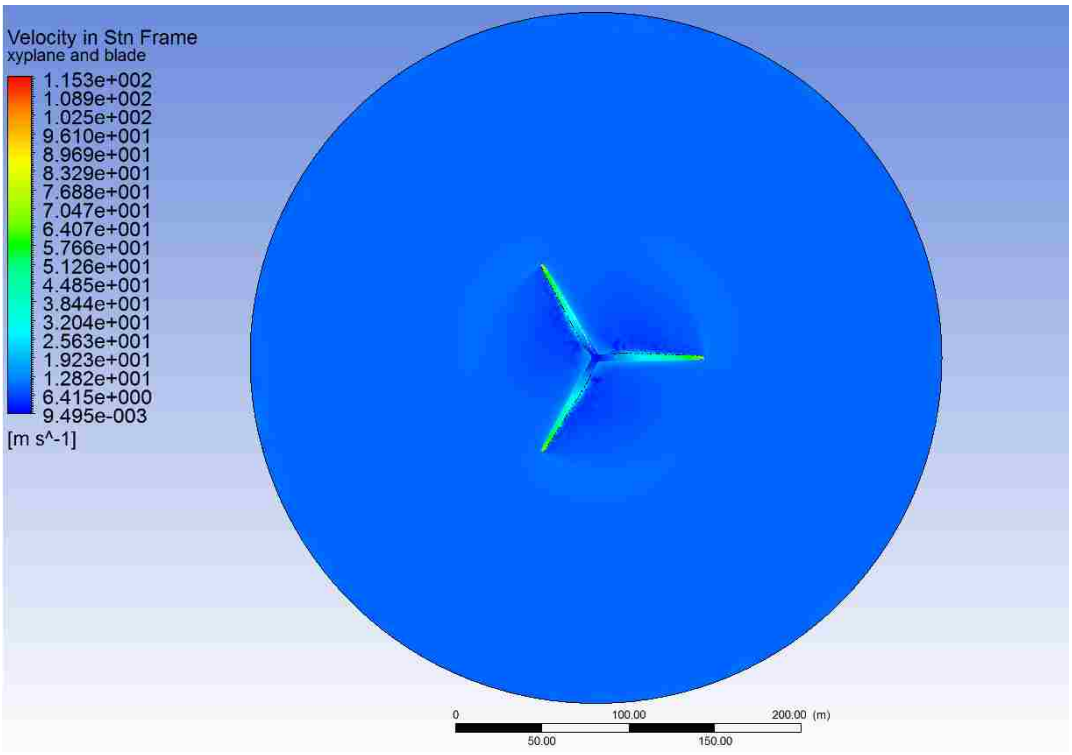


**Figure 5.11 Contour of the rotor and xy-plane at z=0**

Large eddies in this region have complex three dimensional structures. Flow near the leading edge of the blade is free of large eddies. The intensity of turbulence is greatly reduced in the region closer to the hub, as seen in figure 5.12 and 5.13.

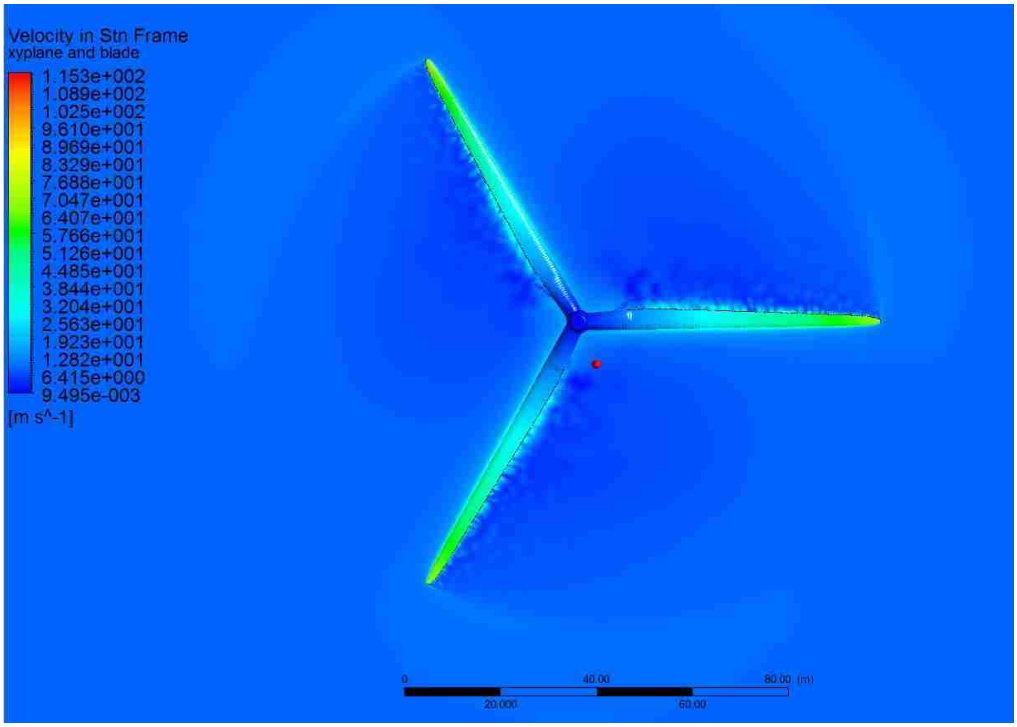


**Figure 5.12 Velocity contours at z = 0 plane – magnified rotor plane**

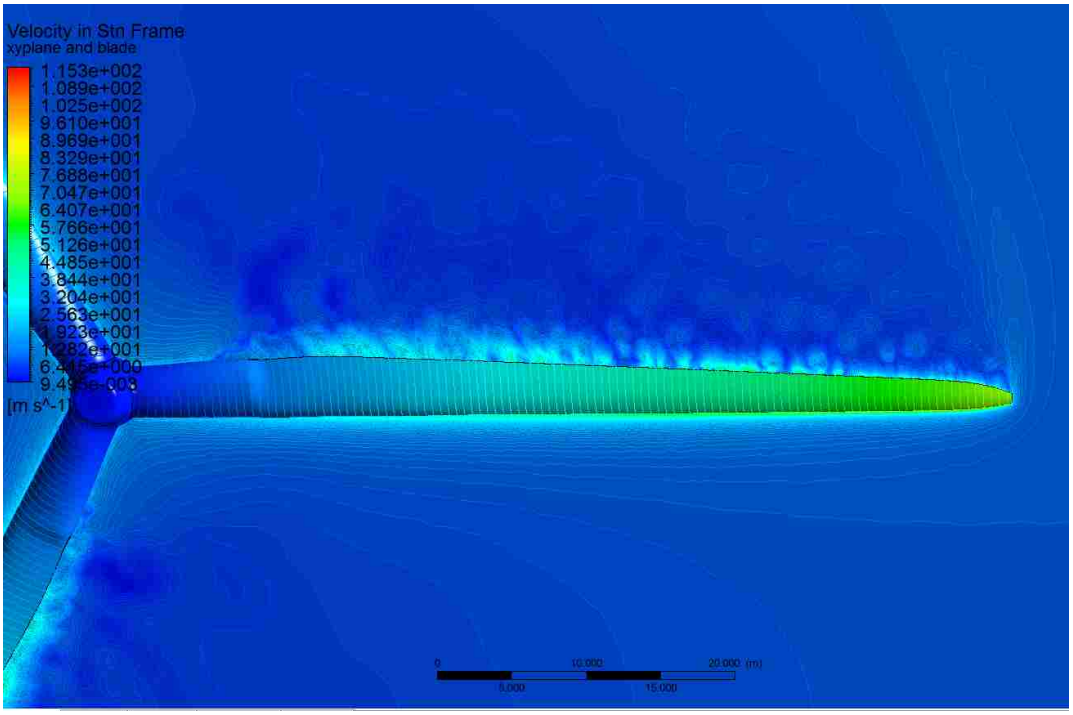


**Figure 5.13 Velocity contours at z = 0 plane – magnified blade region**

The velocity contours of xz-plane at y = 0 are displayed in figure 5.14, 5.15 and 5.16. The flow in the wake of hub and blades is clearly seen in the figures. The wake includes the core region, the transitional region and the fully developed wake region. At the near downstream of the rotor, it is dearly shown that the rotor interacts with incoming potential flow. Near the center, the hub blocks the flow. The highest fluid speed is obtained in the region near the tip of the blades.

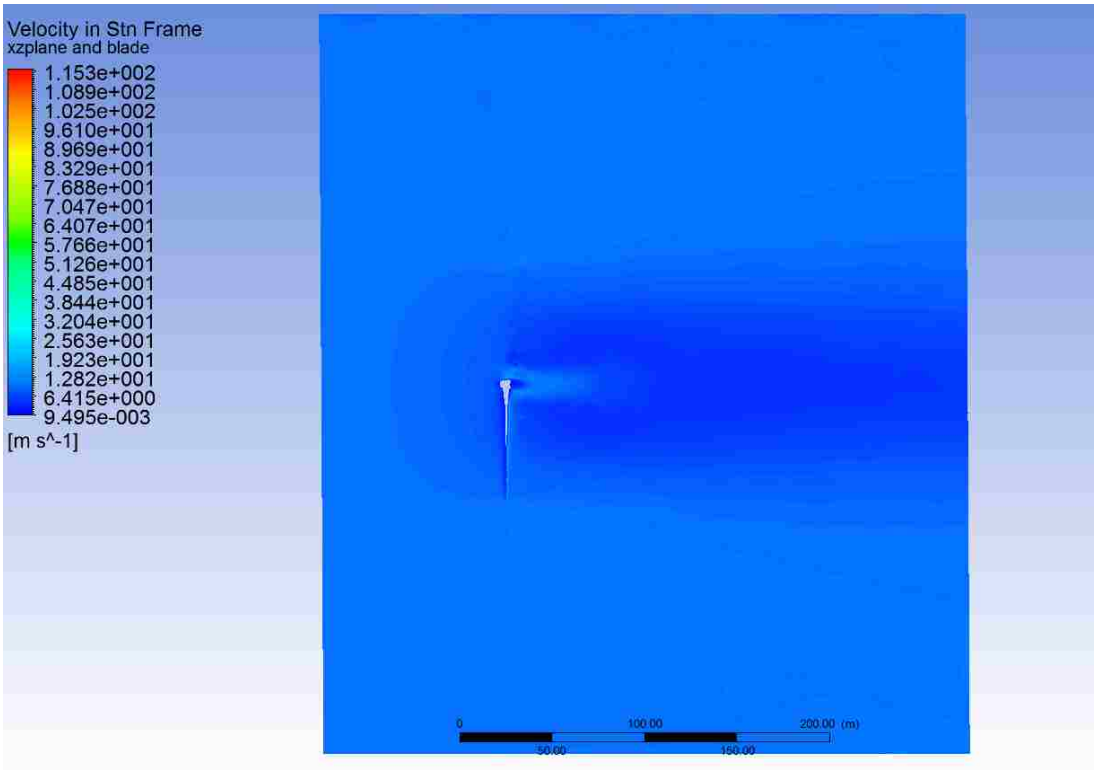


**Figure 5.14 Velocity contours at y=0 plane**

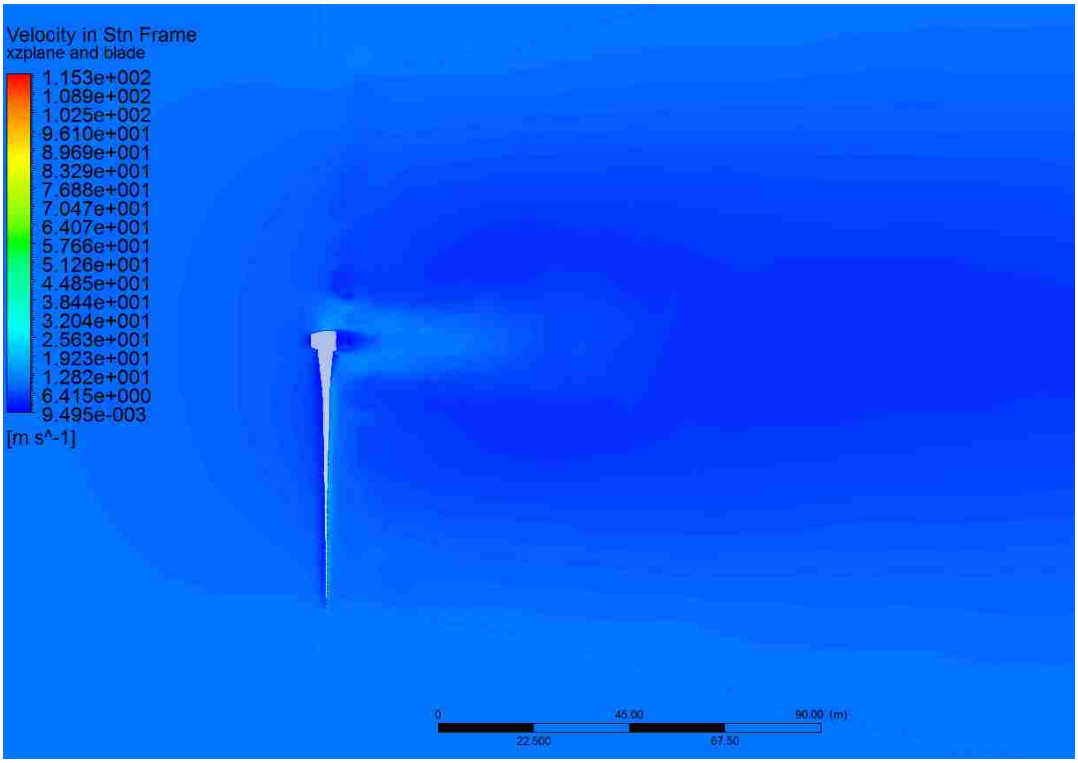


**Figure 5.15 Velocity contours at y = 0 plane - magnified near rotor region**

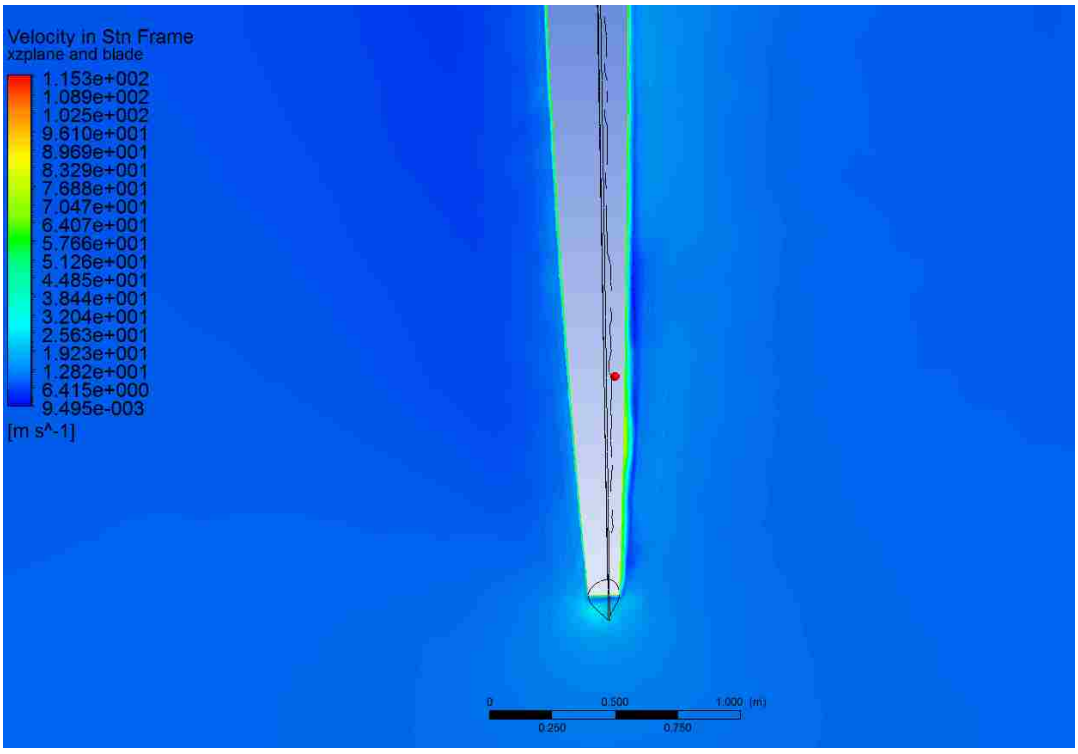


**Figure 5.16 Velocity contours at y = 0 plane – magnified blade region**

Three dimensional velocity vectors at z = 100 m, 0 m, -70 m, -150 m and -250 m planes are shown in figures 5.17 – 5.19. The flow in nearly uniform upstream of the rotor while the wale flow downstream of the rotor is obvious from the distribution of the velocity vectors at these planes. Velocity contours near the rotor region show the complex three dimensional flow structures.

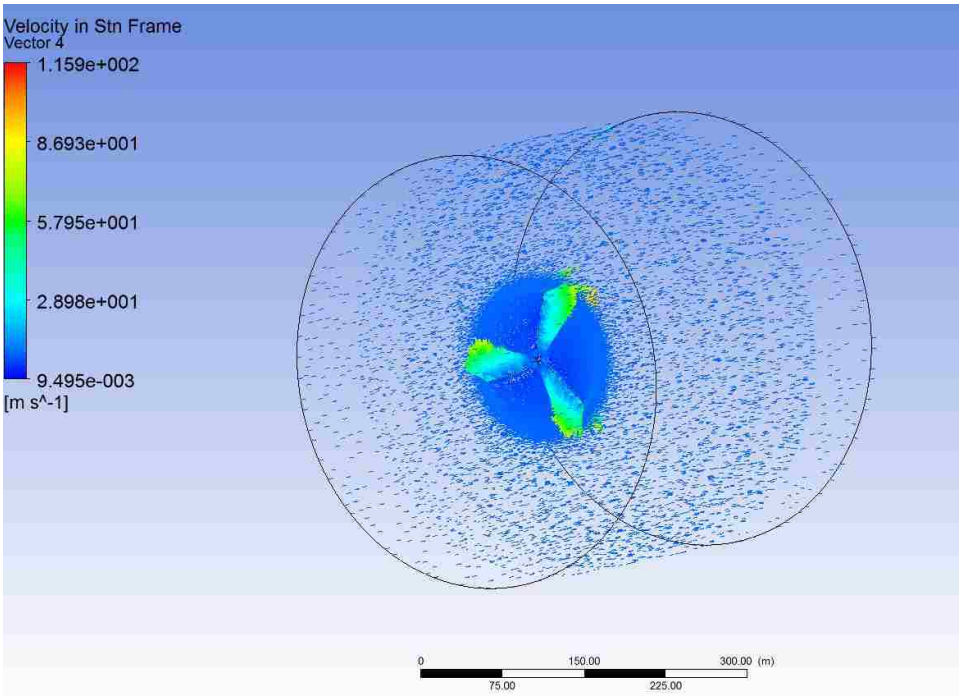


**Figure 5.17 Velocity vectors at z = 100 m, 0 m, -70 m, -150 m and -250 m planes – Front view**

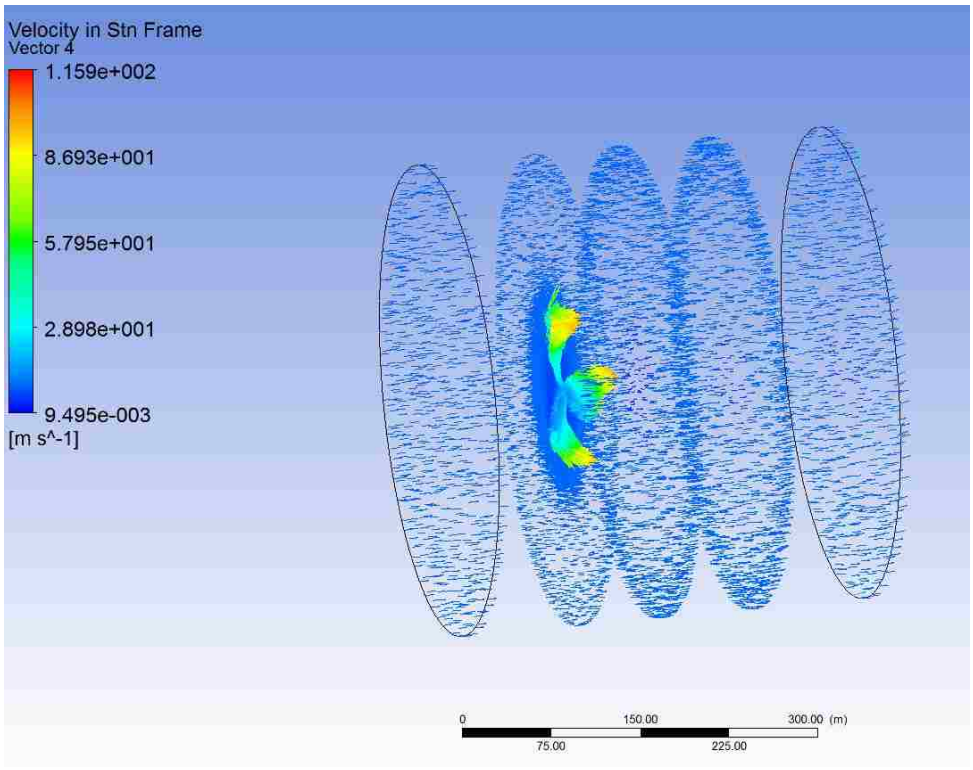


**Figure 5.18 Velocity vectors at z = 100 m, 0 m, -70 m, -150 m and -250 m planes – Back view**

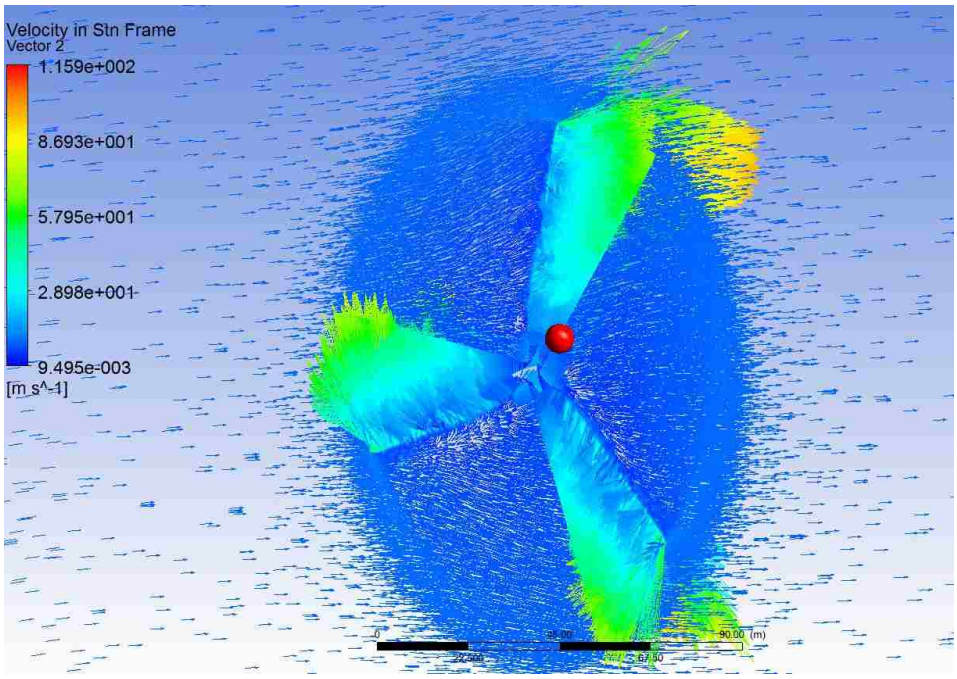


**Figure 5.19 Velocity vectors near the rotor region**

Isosurfaces of the vortices with constant velocity 9.7 m/s at t = 128.525s are shown in figure 5.20 and 5.21. The vortices are initiated from the tip of each blade and are convected downstream. They decayed rapidly away from the blade region, as shown in figures 5.20 and 5.21.

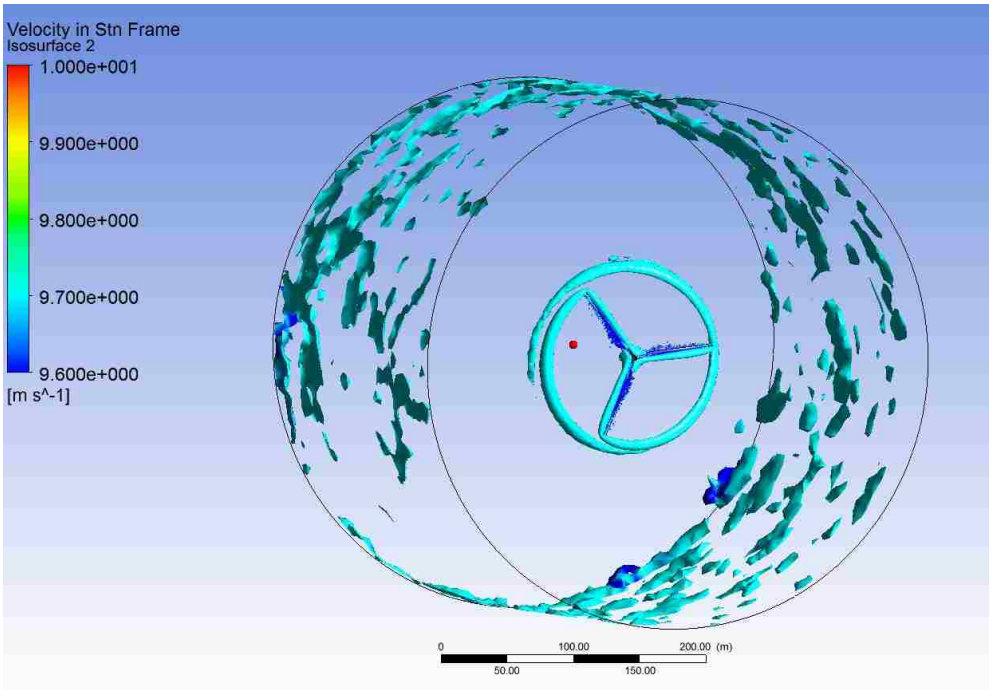


**Figure 5.20 Vorticity isosurfaces of 9.7 m/s speed fluid**

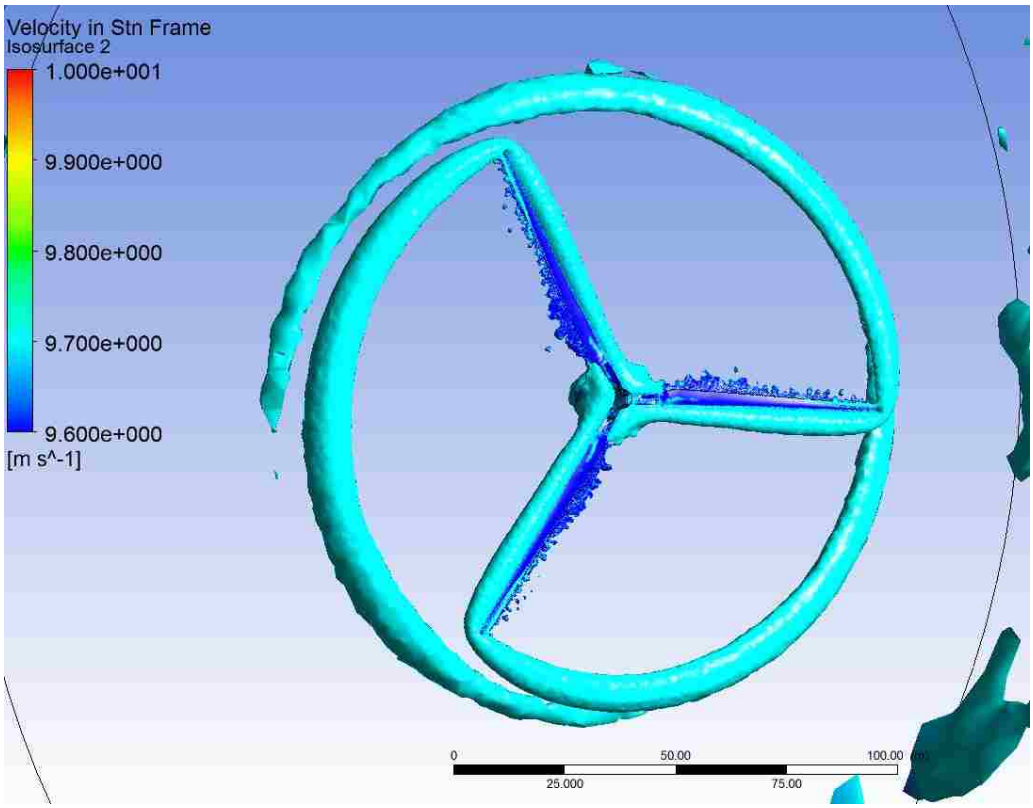


**Figure 5.21 Vorticity isosurfaces near the rotor region**

Static pressure contours along the surface of the blades are shown in figures 5.22 and 5.23. As expected, static pressure is higher along the surfaces at the leading edge than that along the surfaces at the trailing edge.

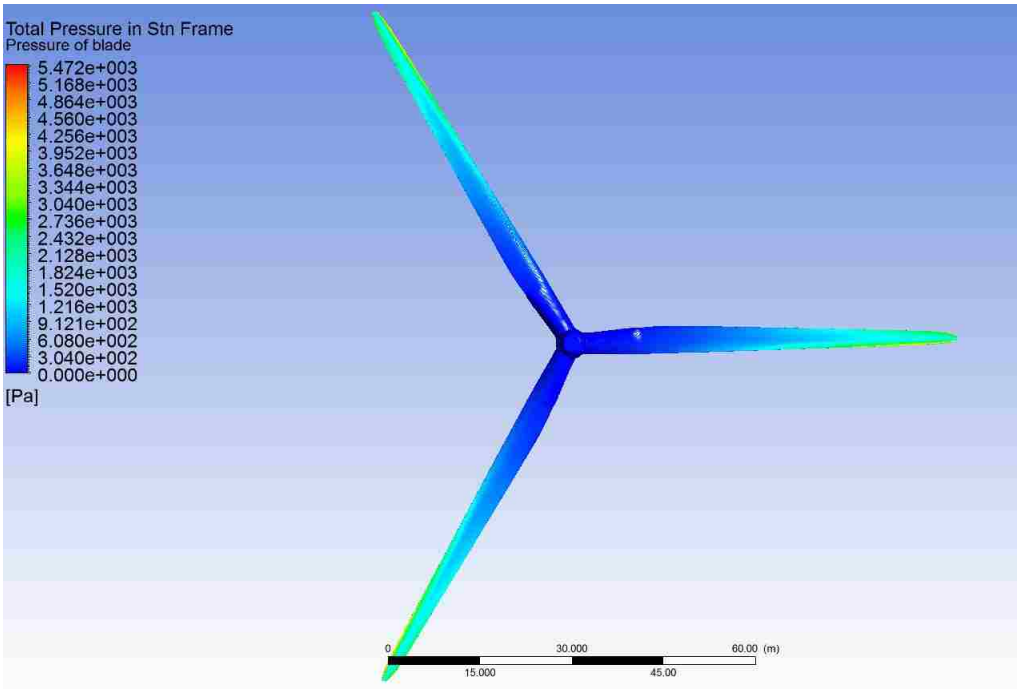


**Figure 5.22 Static pressure field along the surface of the blade**

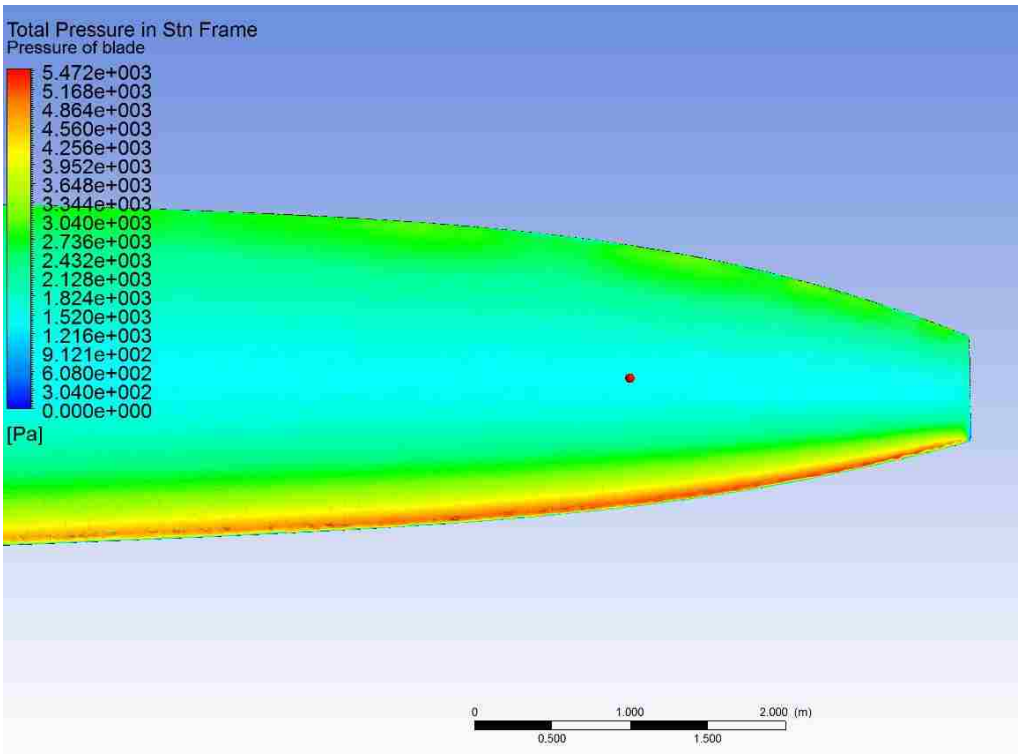


**Figure 5.23 Static pressure distribution near the tip of the blade**

Distributions of the wall shear stress along the surface of the blades are shown in figures 5.24 and 5.25. Low wall shear stress is obtained along the surface of the blade everywhere except the tip region of the blades.

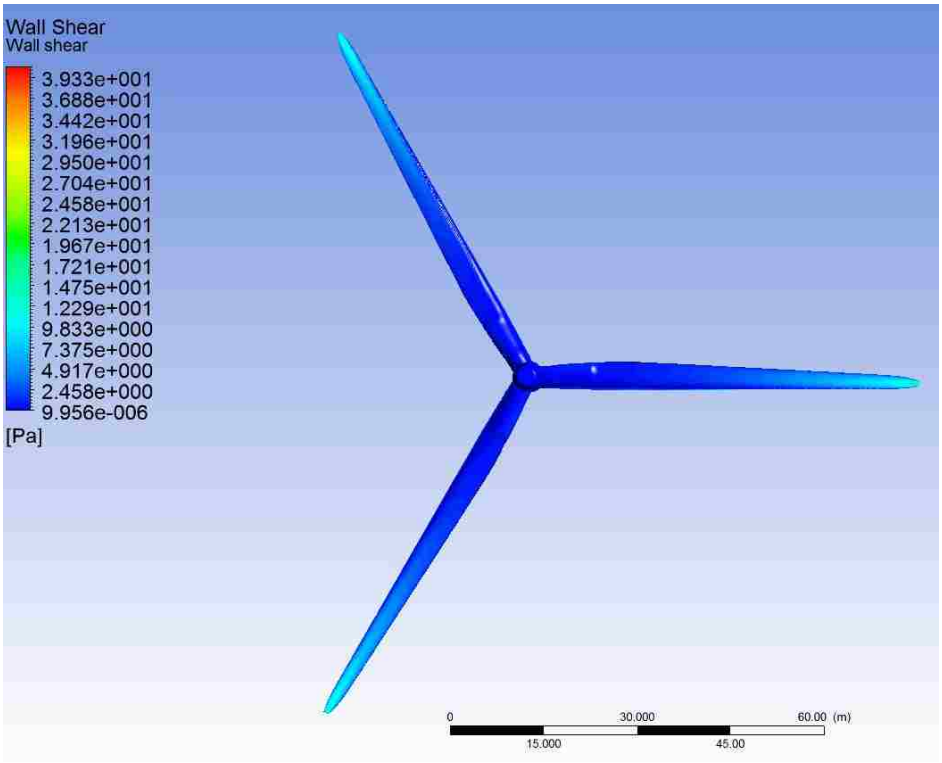


**Figure 5.24 Wall shear of whole rotor**

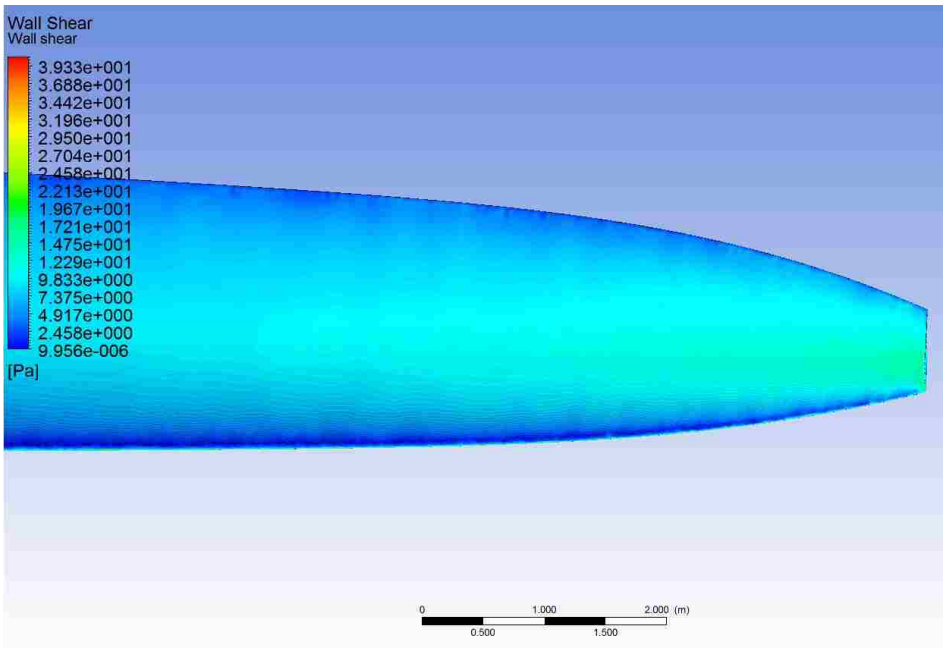


**Figure 5.25 The wall shear stress near the tip of the blade**

# 6. Conclusion

Transient three dimensional turbulent flow simulations are performed for NREL 5 MW offshore baseline wind turbine. Large eddy model is used to solve equations governing the turbulent flow near and far field of the rotor. The spatial structure of the turbulent flow is characterized by examining velocity, pressure and stress fields. The aerodynamic torque and power produced by the wind turbine is calculated.

Outer diameter of the computational fluid domain is selected three times larger than the diameter of the rotor to ensure that potential flow is obtained away from the rotor region. The total length of the computation domain is 350 m long with the length of the upstream of the blade region is 100 m long. The length of the computation domain is chosen to be this long to reduce the effect of the inlet and outlet conditions on the torque and power generated by the turbine and the flow structure near the rotor region. The present simulation includes the whole rotor region while previous investigators only consider one third of the rotor region in their simulations. Hence the simulations presented here better represent the actual wind turbine operations.

Large eddy simulation method is proven to be a reliable tool to study complex transient turbulent flows. As air flow in the present work is an incompressible flow, the closure of the Reynolds averaged equations is used for this calculation. Simulations are conducted in the reference frame rotating with the rotor. The velocity and vorticity field presented here is transformed back to the stationary frame. For the wind speed of 9 m/s the torque generated by the wind turbine is predicted to be 1,806 kNm.

The power generated by the wind turbine is calculated to be 1.95 MW. The wind turbine designed by the present author generates 72.2 % of the maximum potential power. It is clearly indicated here the torque generated and the flow field presented are the results of fully converged simulations.

# 7. Reference


[1] Walter Musial, Bonnie Ram, "Large-Scale Offshore Wind Power in the United States," *National Renewable Energy Laboratory*, September 2010.

[2] Kooijman HJT, Lindenburg C, Winkelaar D, van der Hooft EL, "DOWEC 6 MW pre-design: Aero-elastic modelling of the DOWEC 6 MW pre-designin PHATAS.," Technical Report DOWEC-F1W2-HJK-01-046, 2003.

[3] J. Jonkman, S. Butterfield, W. Musial, and G. Scott, "Definition of a 5-MW Reference Wind Turbine for Offshore System Development," Technical Report NREL/TP-500-38060, National Renewable Energy Laboratory, 2009.

[4] Y. Bazilevs, M.-C. Hsu, I. Akkerman, S.Wright, K. Takizawa, B.Henicke, T. Spielman and T. E. Tezduyar, "3D simulation of wind turbine rotors at full scale. Part I: Geometry modeling and aerodynamics," *International Journal for Numerical Methods in Fluids*, 2010.

[5] John C. Tannehill, Dale A. Anderson, Richard H. Pletcher, Computational Fluid Mechanics and Heat Transfer, Second Edition, Taylor & Francis, 1997.

[6] ANSYS, "ANSYS FLUENT 12.0 Theory Guide," ANSYS, Inc., April 2009.

[7] J. O. Hinze, "Turbulence," McGraw-Hill, 1975.

[8] P. R. Wolton, “Wind Farm Wake Prediction Using CFD,” UMI Microform, 2008.

# 8. Appendices

## 8.1 Appendix A: Details of Meshing

| Scope | |
|---|---|
| Scoping Method | Geometry Selection |
| Geometry | 9 Edges |
| **Definition** | |
| Suppressed | No |
| Type | Element Size |
| Element Size | 0.3 m |
| Behavior | Soft |
| Curvature Normal Angle | Default |
| Growth Rate | Default |
| Bias Type | No Bias |

**Figure 8.1 Edge sizing of the leading and trailing edges of blade**

| Scope | |
|---|---|
| Scoping Method | Geometry Selection |
| Geometry | 9 Edges |
| **Definition** | |
| Suppressed | No |
| Type | Element Size |
| Element Size | 3.e-002 m |
| Behavior | Soft |
| Curvature Normal Angle | Default |
| Growth Rate | Default |
| Bias Type | |
| Bias Factor | 5. |

**Figure 8.2 Edge sizing of blade tips**

| Sizing | |
|---|---|
| Use Advanced Size Function | On: Proximity and Curvature |
| Relevance Center | Fine |
| Initial Size Seed | Active Assembly |
| Smoothing | Medium |
| Transition | Slow |
| Span Angle Center | Fine |
| Curvature Normal Angle | 12.0 ° |
| Proximity Accuracy | 0.8 |
| Num Cells Across Gap | 3 |
| Min Size | 3.e-002 m |
| Max Face Size | Default (9.7110 m) |
| Max Size | Default (19.4220 m) |
| Growth Rate | Default (1.20 ) |
| Minimum Edge Length | 4.9272e-003 m |
| **Inflation** | |
| Use Automatic Inflation | Program Controlled |
| Inflation Option | Smooth Transition |
| Transition Ratio | 0.272 |
| Maximum Layers | 5 |
| Growth Rate | 1.2 |
| Inflation Algorithm | Pre |
| View Advanced Options | Yes |
| Collision Avoidance | Layer Compression |
| Fix First Layer | No |
| Gap Factor | 0.5 |
| Maximum Height over Base | 1 |
| Growth Rate Type | Geometric |
| Maximum Angle | 140.0 ° |
| Fillet Ratio | 1 |
| Use Post Smoothing | Yes |
| Smoothing Iterations | 5 |

**Figure 8.3 Global sizing settings**

| | |
|---|---|
| **CutCellMeshing** | |
| Active | No |
| **Advanced** | |
| Shape Checking | CFD |
| Element Midside Nod... | Dropped |
| Straight Sided Eleme... | |
| Number of Retries | 0 |
| Extra Retries For Asse... | Yes |
| Rigid Body Behavior | Dimensionally Reduced |
| Mesh Morphing | Disabled |
| **Defeaturing** | |
| Pinch Tolerance | Default (2.7e-002 m) |
| Generate Pinch on R... | No |
| Automatic Mesh Base... | Off |
| **Statistics** | |
| Nodes | 2322690 |
| Elements | 10640778 |
| Mesh Metric | Skewness |
| Min | 5.1746723694901E-07 |
| Max | 0.89837777780736 |
| Average | 0.250517683068645 |
| Standard Deviation | 0.128752457927622 |

**Figure 8.4 Advanced settings**

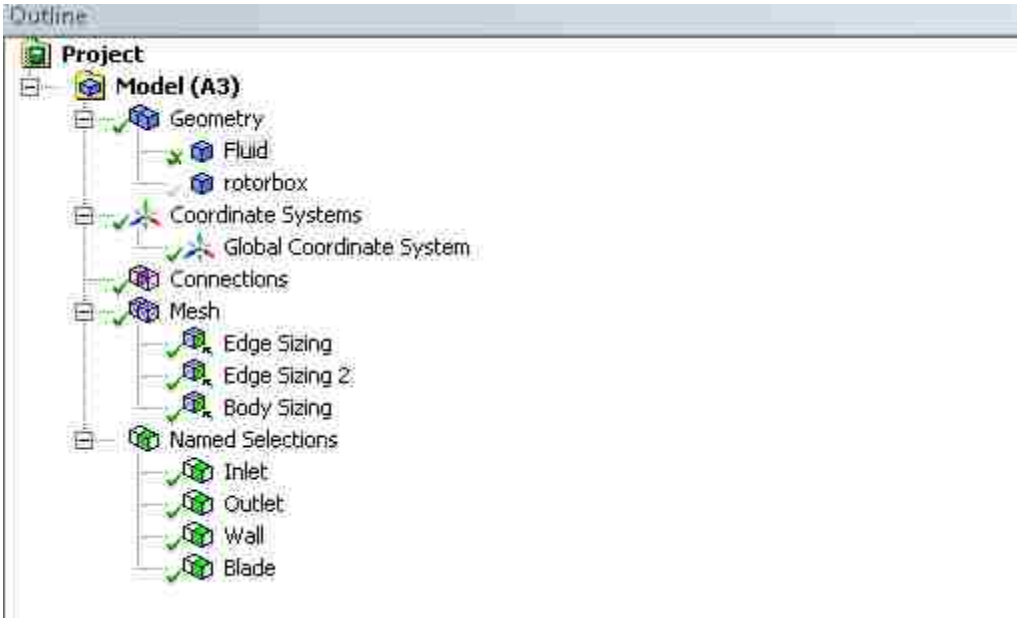


**Figure 8.5 The outline of the sizing**

## 8.2 Appendix B: ANSYS Fluent Settings for Problem Setup

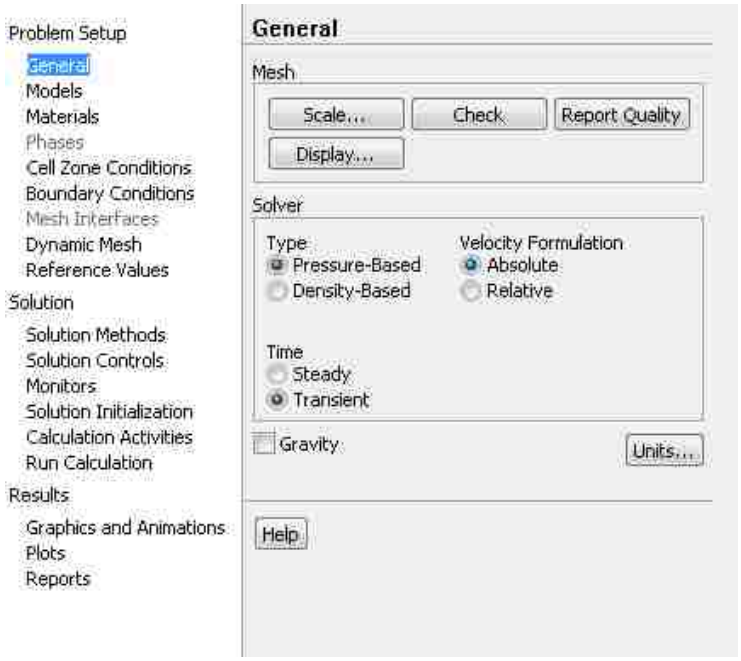


**Figure 8.6 General setup**

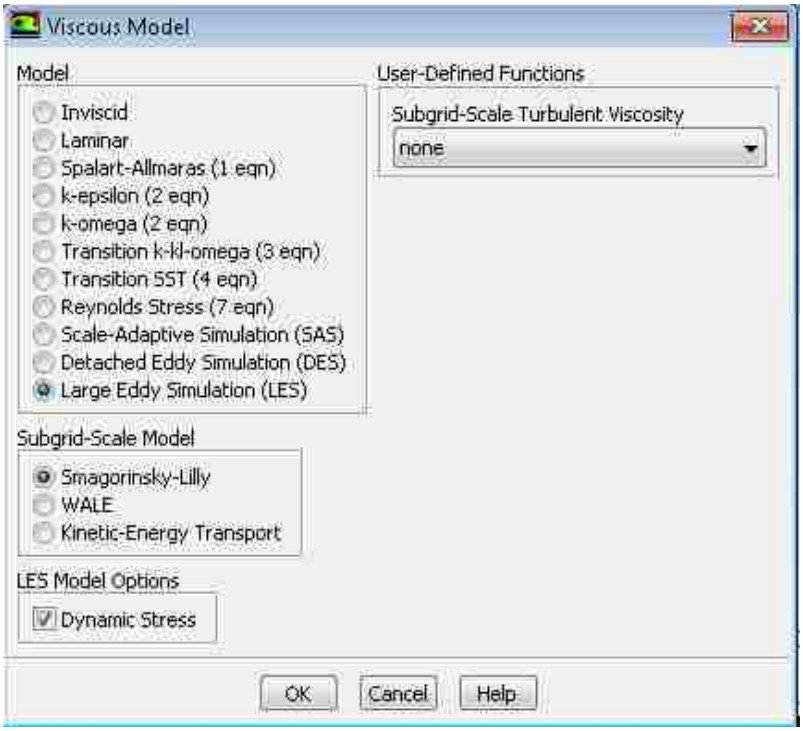


**Figure 8.7 Viscous model**

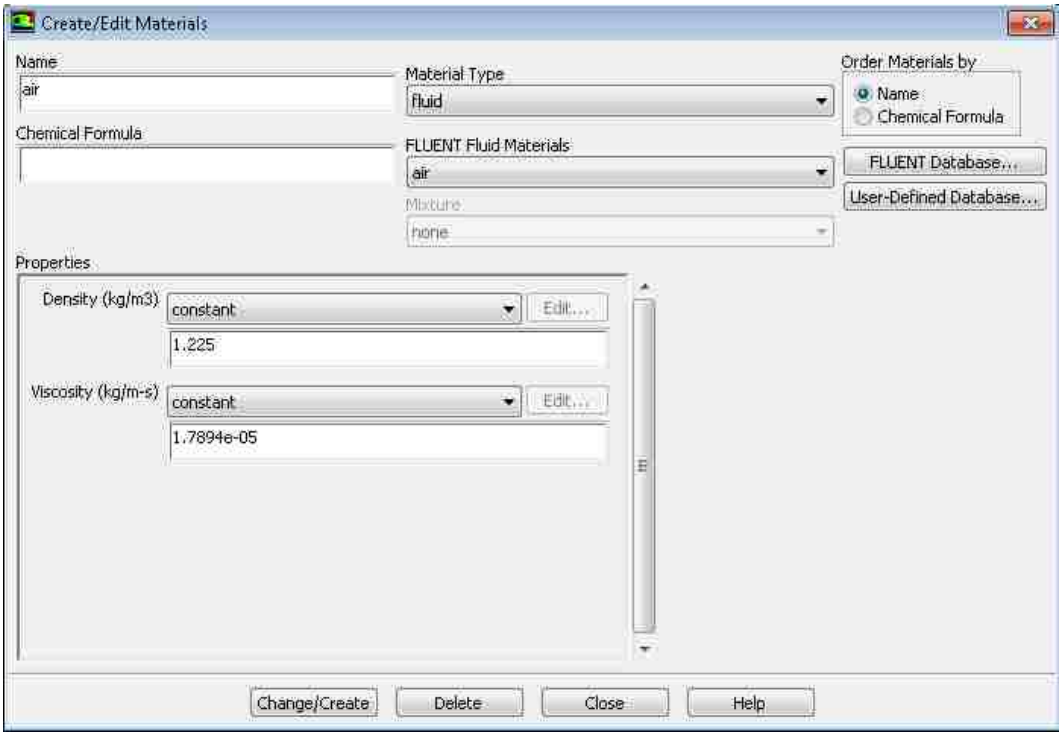


**Figure 8.8 Fluid material**

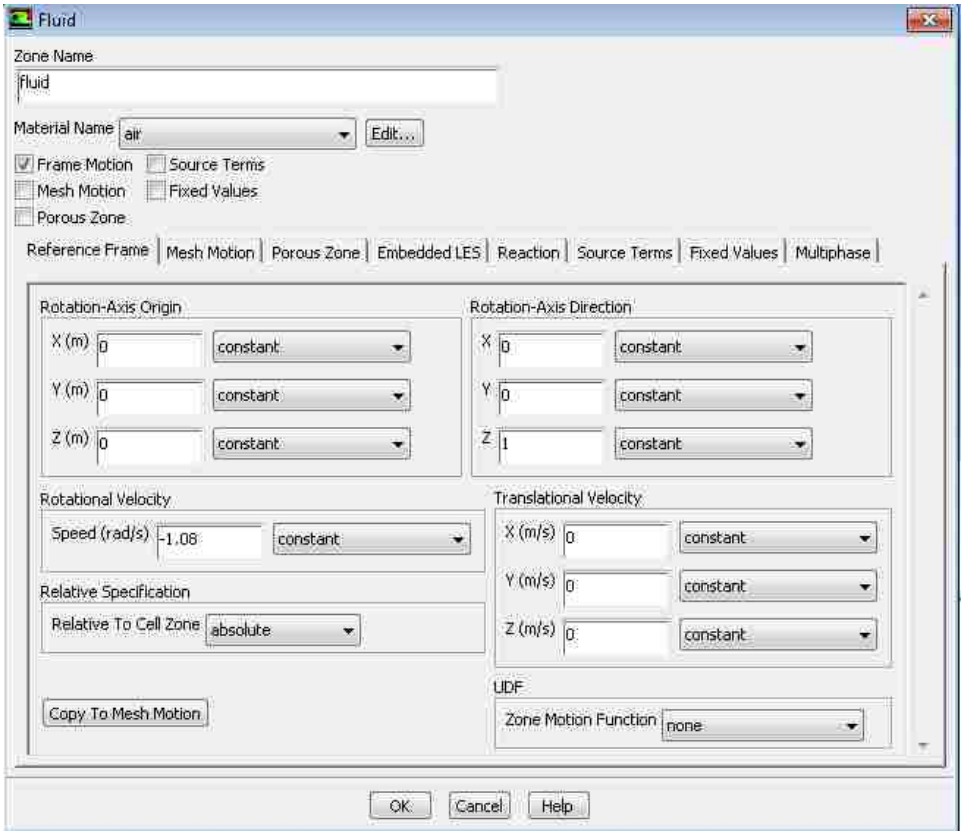


**Figure 8.9 Cell zone settings**

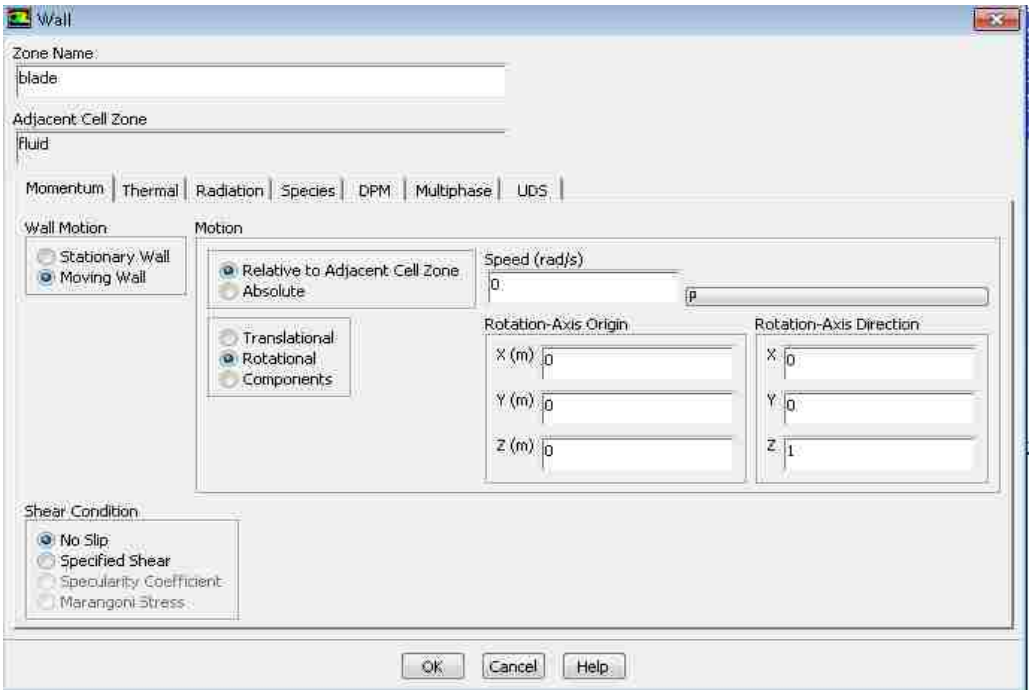


**Figure 8.10 Boundary condition of blade**

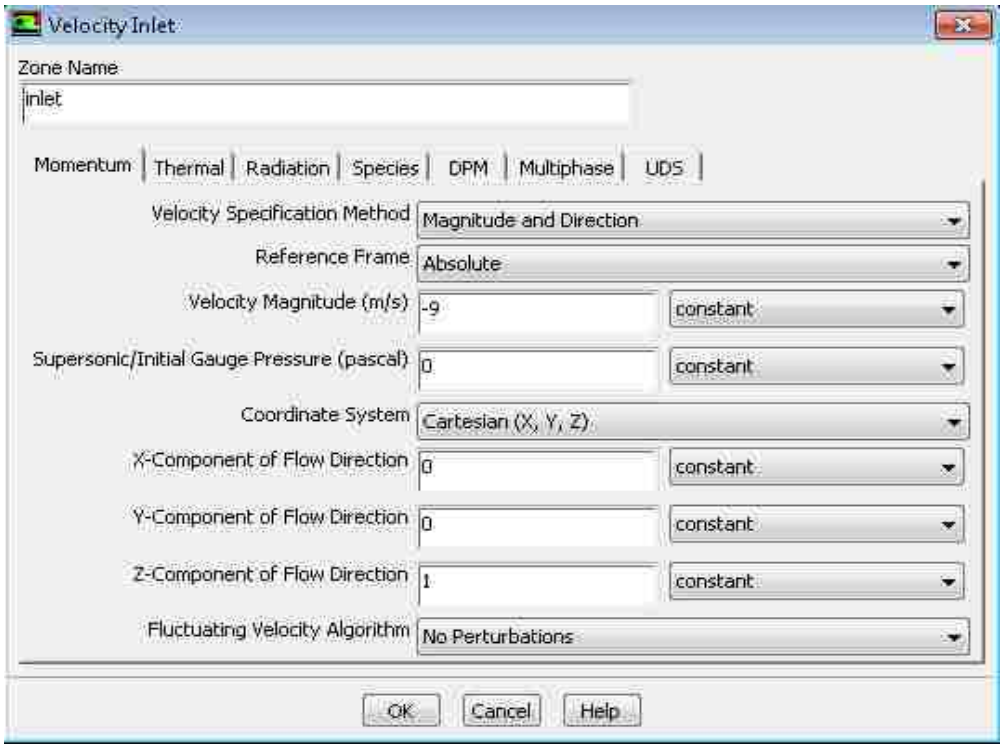


**Figure 8.11 Boundary condition of inlet**

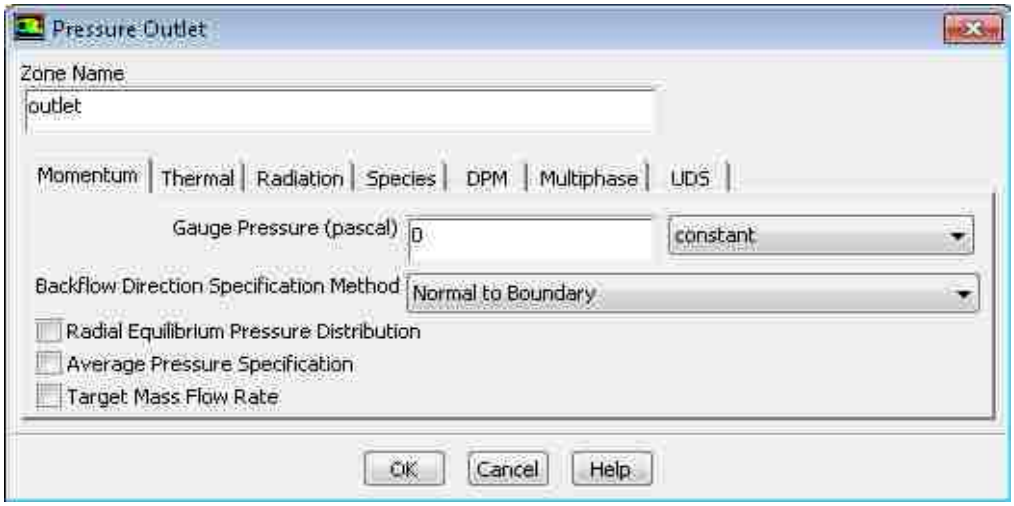


**Figure 8.12 Boundary condition of outlet**

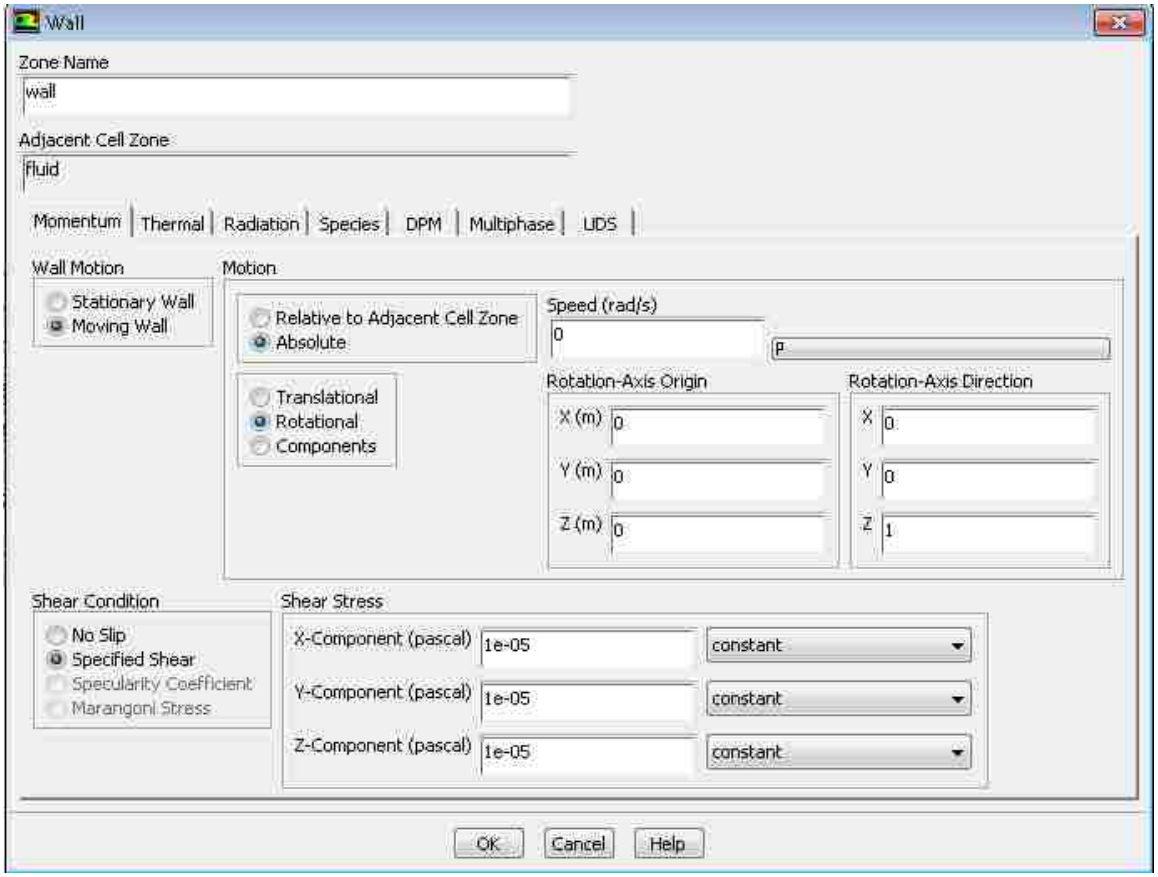


**Figure 8.13 Boundary condition of side wall**

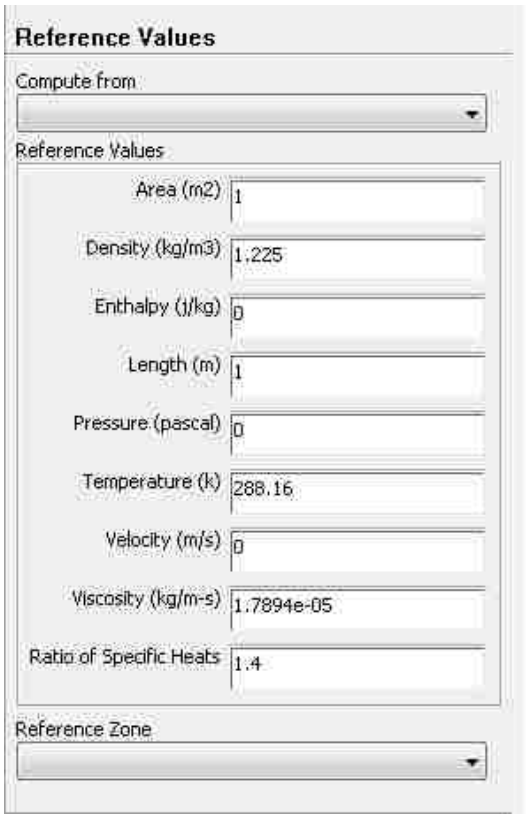


**Figure 8.14 The default reference values**

## 8.3 Appendix C: ANSYS Fluent Settings for Solution Settings

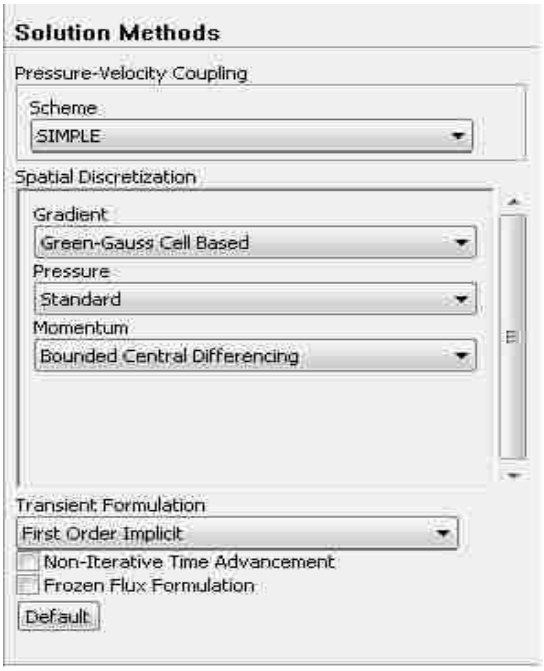


**Figure 8.15 Solution Methods**

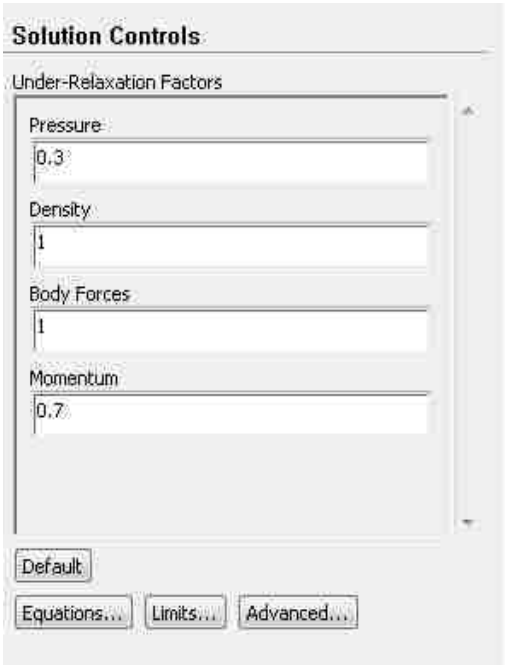


**Figure 8.16 Solution Controls**


**Figure 8.17 Monitors**

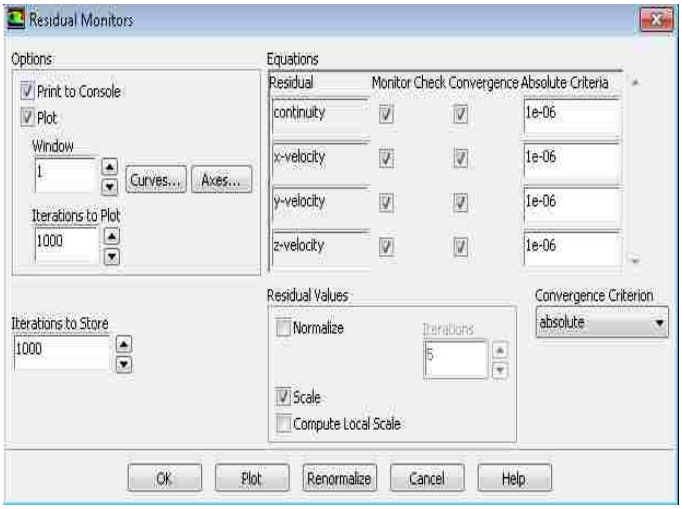


**Figure 8.18 Residual monitors**

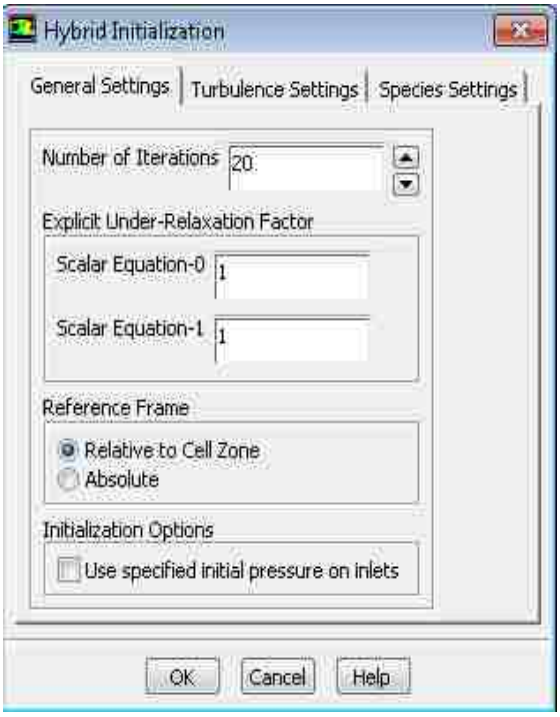


**Figure 8.19 Hybrid initialization**

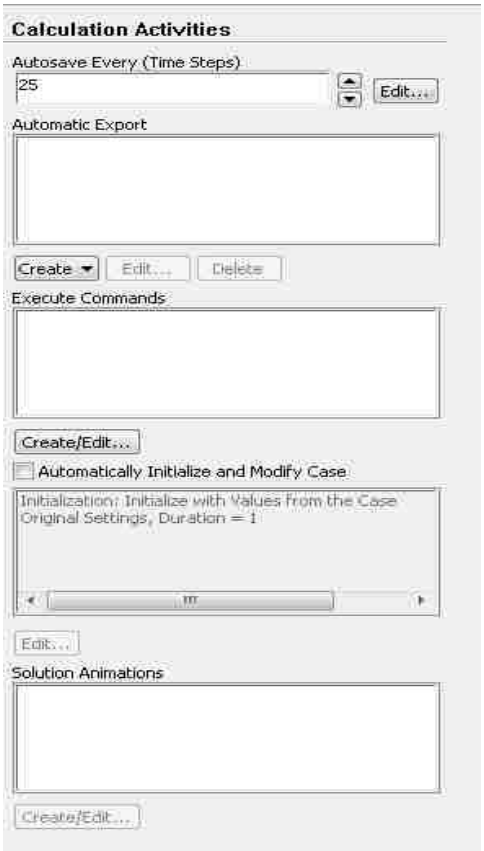


**Figure 8.20 Calculation activities**

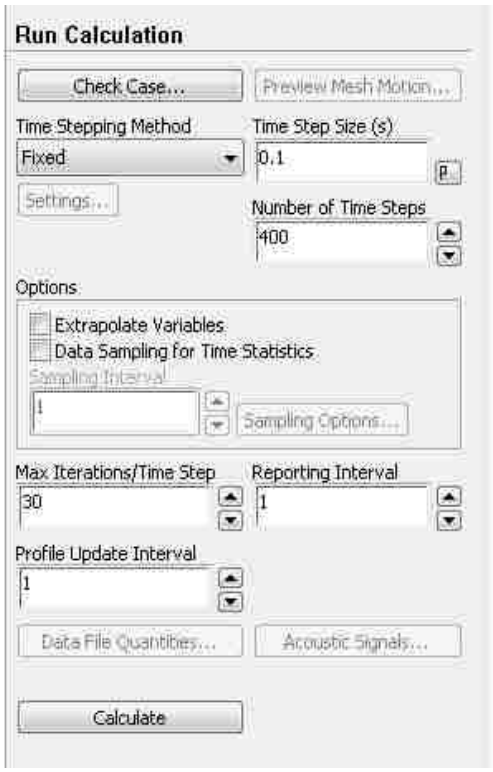


**Figure 8.21 Run calculation**

# 9. Vita

Chenglong Wang was born in Xinghua, Jiangsu Province, China on June, 1988. He attended Hohai University, Changzhou, China from 2006 to 2010 and received a Bachelor of Engineering in Mechanical Engineering and Automation in 2010. In 2012 he earned a Master of Science in Mechanical Engineering at Lehigh University, Bethlehem, PA.